

1 **Fault-controlled dolomitization in the Montagna dei Fiori Anticline (Central Apennines,**
2 **Italy): Record of a dominantly pre-orogenic fluid migration**

3 Mahtab Mozafari¹, Rudy Swennen², Fabrizio Balsamo¹, Hamdy El Desouky^{2,3}, Fabrizio Storti¹
4 and Conxita Taberner⁴

5

6 *1- NEXT - Natural and Experimental Tectonics Research Group - Department of Chemistry,*
7 *Life Sciences and Environmental Sustainability, University of Parma, Italy.*

8 *2- Department of Earth and Environmental Sciences, KU Leuven, Belgium.*

9 *3- Geology Department, Faculty of Science, Menoufia University, Menoufia, Egypt*

10 *4- Shell Global Solutions International B.V., Amsterdam, The Netherlands*

11 Correspondence: Mahtab Mozafari (mahtab_mozafari@yahoo.com) and Fabrizio Storti
12 (Fabrizio.Storti@unipr.it)

13

14 **Abstract**

15 The Lower Jurassic platform and basinal deposits exposed in the Montagna dei Fiori
16 Anticline (Central Apennines, Italy) are pervasively affected by dolomitization. Based on the
17 integration of field work, petrography, and geochemistry, two fault-related dolomitization events
18 were recognized and interpreted as having occurred before and during the Apenninic orogeny,
19 respectively. Fluid inclusion analysis indicates moderate to elevated salinity values of 3.5 to 20.5
20 and 12.8 to 18.6 eq. wt. % NaCl, in the first and the second event, respectively. The estimated
21 salinities, in combination with $\delta^{18}\text{O}$ values and $^{87}\text{Sr}/^{86}\text{Sr}$ ratios, suggest significant involvement
22 of evaporitic fluids in both events, most likely derived from the underlying Upper Triassic
23 Burano Formation. In addition, the $^{87}\text{Sr}/^{86}\text{Sr}$ ratios up to 0.70963 suggest the circulation of deep-
24 sourced fluids that interacted with siliciclastic rocks and/or the crystalline basement during the
25 dolomitization events.

26 Two major dolomite types (D1 and D2) were recognized as pertaining to the first event,
27 both postdated by high amplitude bed-parallel stylolites, supporting a syn-burial, pre layer-
28 parallel shortening dolomitization. A possible geodynamic framework for this dolomitization
29 event is Early to Late Jurassic rift-related extensional tectonism. The second dolomitization
30 event (D3, D4 and D5) is characterized by a temperature upturn (up to 105°C), and interpreted as
31 associated with the inflow of hydrothermal fluids, possibly related to major changes in the

32 permeability architecture of faults during early- to syn-thrusting and folding activity. Based on
33 the timing of deformation in the Montagna dei Fiori Anticline, the second dolomitization event
34 likely occurred in Late Miocene to Pliocene times. The findings regarding characteristics and
35 timing of dolomitization here illustrates the long-term controlling role of the evaporitic
36 detachments in dolomitization process. This study shows that the Mg-rich fluids that were most
37 likely derived from evaporites may prime the tectonically involved successions for repeated
38 dolomitization, and hence formation of potential reservoirs during sequential tectonic
39 modifications (extensional vs. compressional).

40 **1 Introduction**

41 Fault-controlled dolomitization has been the focus of attention in many studies during the last
42 decades due to its influential role in modifying the petrophysical properties of rocks and, hence,
43 anisotropy in fluid migration pathways, and, ultimately on reservoir quality (e.g. Purser et al.,
44 1994; Montanez, 1994; Zempolich and Hardie, 1997; Vandeginste et al., 2005; Davies and
45 Smith, 2006; Sharp et al. 2010). The mechanical and hydrological behaviour of fault zones are in
46 turn influenced by fluid-rock interactions and diagenetic modifications (e.g. Gale et al., 2004;
47 Laubach et al., 2010; Clemenzi et al., 2015; Ferraro et al., 2019). It follows that the mutual
48 interplay between fault activity and rock-fluid interaction can trigger dolomitization of
49 carbonates when exposing to Mg saturated or oversaturated fluids and, consequently, variations
50 in physico-chemical properties of fluids through time and space.

51 Leaking or sealing behaviours of fault zones during deformation are key controls for fault-
52 related fluid circulation. A detailed understanding of such an interplay is thus necessary to
53 improve our capability of making reliable predictions of fault-related dolomitization in carbonate
54 reservoirs. Studying outcrop analogues provides fundamental support to meet this requirement,
55 and the opportunity to assess the spatial distribution of dolomitized zones, and individual
56 diagenetic events, in 3D (e.g. Swennen et al., 2012; Dewit et al., 2014; Bistacchi et al., 2015).

57 The Lower Jurassic to Lower Cretaceous Umbria-Marche passive margin carbonate
58 succession, in the Central Apennines (Italy), is intensely affected by localized dolomitization
59 both in the onshore fold-and-thrust belt and in offshore foredeep and foreland areas (e.g. Murgia
60 et al., 2004; Pierantoni et al., 2013). The dolomitized intervals which are the focus of this study
61 are well-exposed in the core of the Montagna dei Fiori Anticline, where the dolomitized Lower
62 Jurassic intervals (Calcare Massiccio, Bugarone and Corniola Formations) and their relationships

63 with fault zones allow to study the mutual influence between deformation structures and
64 dolomitized intervals (Fig. 1). These intervals, known as the Castel Manfrino Dolostones
65 (Crescenti, 1969; Mattei, 1987; Koopman, 1983), have been previously studied by Ronchi et al.
66 (2003) only at its reference section, exposed at the Castel Manfrino location (Fig. 1b), in the
67 central sector of the Montagna dei Fiori Anticline (Fig. 2). A fault-controlled dolomitization
68 model and the relative timing of dolomitization were proposed by the latter authors based on the
69 homogenization temperatures obtained from microthermometry of the fluid inclusions, and their
70 relation with the thermal history of the area studied. However, no clear relation between
71 dolomitization and structural evolution of the Montagna dei Fiori Anticline on a local scale was
72 provided to confidently link the occurrence of dolomitization to a particular tectonic event.
73 Moreover, the nature and origin of the dolomitizing fluids were not well constrained. Recent re-
74 evaluation of dolostone distribution in the Montagna dei Fiori Anticline (Storti et al., 2017a),
75 showed that the dimension of the dolomitized geobodies (Fig. 2) is much more significant than
76 what was previously mapped by Mattei (1987). Dolostones are distributed within fault damage
77 zones and in the laterally adjacent carbonate rocks, and in intersection areas between fault sets,
78 for a total area in map view of more than 1.5 km² (Storti et al., 2017a).

79 The structural pattern of the Montagna dei Fiori Anticline documents the overprinting of
80 extensional and contractional deformation along major fault zones. The preserved structural
81 framework in this anticline provides an opportunity to study the direct but complex regional
82 tectonic controls on dolomitization in carbonate successions undergoing multiple deformation
83 events, from rifting to folding and thrusting. This contribution integrates new petrographic,
84 geochemical, and microthermometric analyses, with structural studies (Storti et al., 2018) to
85 characterize the temporal record of fault-controlled diagenetic phases and, more specifically,
86 dolomitization in the carbonatic succession outcropping in the Montagna dei Fiori Anticline.
87 These findings might be of relevance for exploration and reservoir quality prediction in the
88 region of the Apennines and Southern Alps, both onshore and offshore. Moreover, this work
89 provides additional evidence of the potential influence of fluids derived from evaporitic
90 detachment levels in modifications of geochemical trends and petrophysical properties of the
91 overlying carbonate rocks.

92 **2 Geological setting**

93 The Montagna dei Fiori Anticline is a NNW-SSE striking, thrust-related fold located at
94 the mountain front of the Central Apennines (Fig. 1). The geodynamic evolution of the
95 Apennines has been proposed to be the result of the superposition of NE-SW compression (in
96 present-day geographic coordinates), related to the convergence between Eurasia and Africa
97 plates since the Late Cretaceous times (Elter et al., 1975; Dewey et al., 1989; Patacca et al.,
98 1992), on a rifting-related tectono-sedimentary architecture produced by Early Jurassic extension
99 (e.g., Centamore et al., 1971). In such a framework, the Central Apennines developed during
100 Miocene to Plio-Pleistocene times (e.g. Parotto and Praturlon, 1975; Barchi et al., 1998; Mazzoli
101 et al., 2002; Bollati et al., 2012).

102 The Central Apennines involves the Umbria-Marche succession, which essentially
103 includes Triassic to Miocene carbonates and marls, covered by Miocene to Pliocene syn-
104 orogenic clastic sediments (Fig. 1). The pre-orogenic succession, from bottom to top, includes
105 Late Triassic evaporites, dolomites and limestones of the Burano Formation which the basal
106 detachment runs within its evaporitic interval (Ghisetti and Vezzani, 2000), Early to Late
107 Jurassic platform and basinal limestones and dolostones (Calcare Massiccio, Corniola, Rosso
108 Ammonitico, Calcari a Posidonia and Calcari ad Aptici Formations), and Cretaceous to Early
109 Miocene basinal carbonates (Maiolica, Marne a Fucoidi, Scaglia and Biscaro Formations). In
110 general, the lower part of the Burano Formation is overlaid by the fluvio-deltaic siliciclastic
111 rocks of the Verrucano Formation (Middle-Late Triassic) (Tongiorgi et al., 1977; Ghisetti and
112 Vezzani, 2000; Tavani et al., 2008). Nevertheless, the existence of these siliciclastic rocks in the
113 Montagna dei Fiori area is not yet proven. Syn-orogenic deposits include Miocene marls and
114 turbiditic sandstones (Marne con Cerroghna and Laga Formations) (Artoni, 2013 and references
115 therein).

116 The deposition of the Calcare Massiccio Formation (Hettangian-Sinemurian) with a total
117 thickness varying between 300 to 700 m (Pialli, 1971), records an important extension pulse in
118 the evolution of Tethyan rifting. The lower part of this formation which has been interpreted as
119 having been deposited in a peritidal environment consists of peloidal pack- to grainstones in
120 alternation with peloidal wacke- to packstones including horizons of algal bindstones (Calcare
121 Massiccio A; Brandano et al., 2016). The upper part is made up of beds of skeletal and coated
122 grain wacke- to grainstones (Calcare Massiccio B; Brandano et al., 2016). It corresponds to
123 lower to middle shelf depositional environments, characterized by a general deepening-upward

124 trend. Overall, the Early Jurassic rifting led to the growth of the Calcare Massiccio Formation in
125 a carbonate platform setting, followed by faulting and drowning, and development of pelagic
126 intrabasins filled by syn-rift sediments (Fig. 1c; Bernoulli et al. 1979; Santantonio and Carminati,
127 2011). The syn-rift sediments include pelagic limestones of the Bugarone and Corniola
128 Formations. Condensed pelagic limestones of the Bugarone Formation (Lower Pliensbachian-
129 Lower Tithonian; Bugarone Group in Pierantoni et al., 2013) occur at the top of the Calcare
130 Massiccio Formation where it formed fault-controlled highs marking the regional drowning of
131 the carbonate platform (Santantonio and Carminati, 2011). The pelagic limestones of the
132 Corniola Formation (Sinemurian-Toarcian; Colacicchi et al., 1975; Morettini et al., 2002;
133 Bosence et al., 2009; Marino and Santantonio, 2010; Brandano et al., 2016) occur within the
134 fault-controlled (half)grabens in lateral continuation with the Calcare Massiccio Formation. The
135 Corniola Formation in the lower part consists of turbiditic lobes which originated from tectonic
136 brecciation of the Calcare Massiccio Formation. The upper part consists of a well-bedded pelagic
137 mudstone with chert nodules (Di Francesco et al., 2010).

138 **2.1 Structural Framework**

139 The Montagna dei Fiori Anticline is intersected by two major fault categories (Storti et al.,
140 2018), which based on the chronological order include: Firstly, ~ E-W and ~ N-S striking fault
141 zones showing extensional kinematics bounding the major outcrops of Calcare Massiccio and
142 dominantly affecting the Jurassic rocks older than the Maiolica Formation (Fig. 2a, e.g. sites 1 to
143 4). Overprinting relations indicate that ~ E-W deformation structures are systematically younger
144 than the ~ N-S ones. Similar trends were observed in syn-rift fault zones in other anticlines of the
145 Central Apennines (e.g. Cooper and Burbi, 1986; Alvarez, 1989; Chilovi et al., 2002). Such a
146 tectonosedimentary inheritance was involved in the growth of the Montagna dei Fiori Anticline,
147 which initiated during the Late Miocene (Mazzoli et al., 2002; Artoni, 2003) and progressively
148 evolved into the upper thrust sheet of a well-developed antiformal stack until Plio-Pleistocene
149 times (e.g. Ghisetti et al., 1993; Calamita et al., 1994; Artoni, 2013). The second set of faults is a
150 major structural feature trending parallel to the Montagna dei Fiori Anticline and dissecting it is
151 the Montagna dei Fiori Fault, a NNW-SSE striking extensional fault system cutting at a high
152 angle through the folded footwall rocks, typically at the forelimb-crest transition (Figs. 1, 2).
153 This fault consists of two partially overlapping main fault zones with an extensional stratigraphic
154 separation exceeding 900 m, and juxtaposes intensely deformed Late Miocene sediments in the

155 hanging wall, against dolomitized and undolomitized Lower Jurassic and Cretaceous limestones
156 in the footwall (Figs. 1 and 2). The development of the Montagna dei Fiori Fault has been
157 alternatively interpreted as either a pre- (e.g. Calamita et al., 1994, Mazzoli, 2002; Scisciani et
158 al., 2002) or late-folding (Ghisetti and Vezzani, 2000) feature. More recently, the origin of the
159 Montagna dei Fiori Fault has been ascribed to the mutual interaction between horizontal
160 shortening and uplift, and episodic gravitational re-equilibration during antiformal stacking
161 underneath the anticline during Plio-Pleistocene times (Storti et al., 2018). The dolomitized
162 intervals are exposed in the damage zones of the both aforementioned fault categories.

163 **3 Methodology**

164 The fieldwork covered an area of over 4 km² to delineate the distribution of dolostones.
165 The stratigraphic and deformational features of dolostones were analyzed in more than 60
166 outcrops. The distribution of dolomitized intervals as well as their cross-cutting relationships
167 with bedding planes, stylolites, veins and faults were documented and sampled. For petrographic
168 analyses, 130 polished thin sections were studied with standard petrographic methods
169 (transmitted and UV-fluorescent light microscopy). Dolomite crystal morphology and texture is
170 based on the classification proposed by Sibley and Gregg (1987).

171 The rock slabs and thin sections were stained using Alizarine Red S and potassium
172 ferricyanide (Dickson, 1966) to discriminate dolomite from calcite and evaluate their iron
173 content. Cold cathodoluminescence microscopy (CL) was carried out on representative thin
174 sections (n = 80) at KU Leuven University (Belgium) using a Technosyn cathodoluminescence
175 device (8-15 kV, 200-400 μ A gun current, 0.05 Torr vacuum and 5 mm beam width).

176 $\delta^{13}\text{C}$ and $\delta^{18}\text{O}$ analysis were carried out on 117 samples. To ensure the sampling quality
177 and avoid physical mixing of different diagenetic phases, the thin section images were mapped
178 and the sampling targets were determined. Nevertheless, some diagenetic phases could not be
179 isolated due to their sequential overgrowth and small size. Powder samples (150 - 200 μ g) were
180 obtained by applying a New Wave Research micromilling device and a dental drill at KU
181 Leuven University (Belgium). The analysis was conducted at Parma University (Italy) and the
182 Friedrich-Alexander-Universität (Erlangen-Nürnberg, Germany) laboratories using Finnigan
183 DeltaPlus V and ThermoFinnigan 252 mass spectrometers, respectively. The carbonate powders
184 were reacted with 100% phosphoric acid at constant temperature of 75°C. Several additional CO₂
185 reference gases (NBS18, NBS19, MAB99, and a pure Carrara marble) with known isotopic ratio

186 were analyzed during the measurements to determine the $\delta^{13}\text{C}$ and $\delta^{18}\text{O}$ values of the sample.
187 Reproducibility was checked by replicate analysis of laboratory standards and was better than
188 $\pm 0.1\text{‰}$ for $\delta^{13}\text{C}$ and $\pm 0.2\text{‰}$ for $\delta^{18}\text{O}$ at Parma University and ± 0.04 for $\delta^{13}\text{C}$ and $\pm 0.05\text{‰}$ for
189 $\delta^{18}\text{O}$ at Friedrich-Alexander-Universität. Oxygen isotope composition of dolomites was
190 corrected using the acid fractionation factors given by Rosenbaum and Sheppard (1986).
191 Duplicate homogeneous samples measured in both labs for inter-laboratory reproducibility. All
192 carbon and oxygen values are reported in per mil, relative to the “Vienna Pee Dee Belemnite”
193 (V-PDB).

194 A total number of 21 samples were analyzed for their $^{87}\text{Sr}/^{86}\text{Sr}$ ratios. The analyses were
195 conducted at the Department of Analytical Chemistry, Ghent University (Belgium) and at the
196 Vrije Universiteit Amsterdam (the Netherlands). NIST SRM 987 was used as the international Sr
197 standard in both labs. At Ghent University, 15 sample powders (20 mg) were collected using a
198 dental drill device. The $^{87}\text{Sr}/^{86}\text{Sr}$ ratio measurements were performed using a Thermo Scientific
199 Neptune Multi-collector Inductively Coupled Plasma Mass Spectrometer (MC-ICP-MS)
200 instrument. Within the external precision, repeated analyses of the international Sr standard
201 yielded an average $^{87}\text{Sr}/^{86}\text{Sr}$ ratio of 0.710271 ± 0.000023 (2SD, $n = 43$), in agreement with the
202 accepted $^{87}\text{Sr}/^{86}\text{Sr}$ ratio of 0.710248 for this reference sample (Thirlwall, 1991). At Vrije
203 Universiteit Amsterdam, 6 sample powders (2 - 3 mg) were collected using a New Wave
204 Research micromilling device. Analyses were performed using a ThermoElectron Triton plus
205 TIMS instrument. In order to monitor and document the system’s performance, repeated analyses
206 of the international Sr standard ($n = 58$) were carried out on load sizes of 10 ng and 100 ng which
207 yielded average $^{87}\text{Sr}/^{86}\text{Sr}$ ratios of 0.710245 ± 0.000022 (2SD) and 0.710242 ± 0.000008 (2SD),
208 respectively. In both labs mass discrimination correction was performed via internal
209 normalization using Russell’s exponential law and the accepted value (0.1194; Steiger and Jager,
210 1977) of the invariant $^{86}\text{Sr}/^{88}\text{Sr}$ ratio.

211 Fluid inclusion microthermometry analysis was performed on 11 doubly polished wafers
212 (80-130 μm in thickness). Measurements were carried out at Parma University (Italy) using
213 Linkam THMSG-600 and Linkam MDS-600 heating-cooling stages coupled with a Leica DM
214 2500 microscope. The final melt (T_{mice}) and homogenization temperatures (T_{h}) were
215 reproducible within 0.5°C and 5°C , respectively. The stages were calibrated by synthetic Syn
216 FliTM fluid inclusion standards. A 100x objective was used during the microthermometry runs

217 of the small inclusions. The microthermometry data were collected following the Fluid Inclusion
218 Assemblage (FIA) approach described in Goldstein and Reynolds (1994) for carbonate minerals.
219 The inconsistent homogenization temperatures and salinities obtained for these fluid inclusions,
220 within the framework of an individual fluid inclusion assemblage (FIA) described by Goldstein
221 and Reynolds (1994), indicate possible re-equilibration (stretched) of these inclusions and thus
222 are not used in the interpretations. It is common for small inclusions ($< 3 \mu\text{m}$) to remain mono-
223 phase all-liquid at room temperature due to their metastability (Goldstein and Reynolds, 1994).
224 Thus, to eliminate the possible role of metastability, the samples were placed in a freezer for
225 several days following the procedures described in detail by Goldstein and Reynolds (1994). All-
226 liquid inclusions remained unchanged and no vapor bubble was developed within them, which
227 discards the metastability effect. In order to properly observe the phase transitions and determine
228 the final melting temperature of ice in the all-liquid inclusions, they were rapidly heated up to
229 $\sim 200^\circ\text{C}$ to stretch and nucleate a bubble at room temperature (Goldstein, 1990). The salinities
230 are reported in equivalent weight percent NaCl (eq. wt. % NaCl) and were calculated based on
231 the equation of Bodnar (1993). The homogenization temperatures obtained in all fluid inclusion
232 assemblages indicate the minimum temperatures at which the fluids could have been trapped
233 (Goldstein and Reynolds, 1994). No correction was made for pressure effects on entrapment
234 temperatures since no data regarding the exact depth and pressure of entrapment are available. In
235 absence of independent thermal indicators such as Conodont Alteration Index (CIA) and
236 Vitrinite Reflectance (VR), the accuracy of pressure correction cannot be well constrained
237 (Slobodník et al, 2006), and thus no correction was made for pressure effects on homogenization
238 temperatures.

239 In order to perform high resolution petrography, Scanning Electron Microscope (SEM)
240 and Back-scattered Scanning Electron Microscope (BSEM) analyses were conducted using a
241 Jeol 6400 Scanning Electron Microscope (SEM) equipped with an Oxford EDS (Energy
242 Dispersive System). Operating conditions were 15 kV and 1.2 nA, electron beam about $1 \mu\text{m}$ in
243 diameter and 100 s counting time; errors are $\pm 2\text{-}5\%$ for major elements and $\pm 5\text{-}10\%$ for minor
244 components. The analysis focused mainly on detecting possible dolomite crystals inside the bed-
245 perpendicular stylolites affecting the Cretaceous Scaglia Formation.

246 **4 Results**

247 **4.1 Field observation and distribution of the dolomitized bodies**

248 There is no evidence of dolomitization in the overlying and immediate surrounding
249 successions of the Calcare Massiccio, Bugarone and Corniola Formations (e.g. Maiolica and
250 Scaglia Formations), though the base of Maiolica Formation is reported as dolomitized in the
251 Central Apennines onshore (e.g. Pierantoni et al., 2013) and offshore areas (Murgia et al., 2004).

252 Dolomitized intervals are folded in the forelimb of the Montagna dei Fiori Anticline and
253 are abruptly truncated by the Montagna dei Fiori Fault, which juxtaposes them against intensely
254 foliated Scaglia, Bisciaro and Marne con Cerroghna Formations (Figs. 2 and 3). The distribution
255 of dolomitized intervals is wider in the Salinello creek (Figs. 1b, 2a) perhaps due to a better
256 exposure. In the Corano Quarry location, dolomitization occur in the Calcare Massiccio and
257 Bugarone Formations only as meter-sized dolostone geobodies in the footwall of the Montagna
258 dei Fiori Fault (Fig. 4). The map pattern (Fig. 2) of dolostones indicates that their distribution is
259 maximized in the Castel Manfrino-Osso Caprino hill area and fades out both southward and
260 eastward.

261 The lateral extent of dolomitization is gradual. In some outcrops, dolomitization fronts
262 show irregular outlines following, but also cross-cutting bedding surfaces (Fig. 5). Dolomitized
263 intervals vary in thickness from a few meters to hundred meters affecting the totality of the
264 exposed Calcare Massiccio and the lower part of Corniola Formation, where no clay interlayers
265 are present. In the Calcare Massiccio Formation, dolomitization does not follow a systematic
266 pattern. In the northern side of the Osso Caprino hill (Fig. 2), the top of formation is dolomitized
267 but moving toward the Salinello creek, a thick non dolomitized limestone is exposed. The same
268 situation occurs on the opposite side of the creek and to the east of Castel Manfrino.

269 Dolomitized intervals in the Corniola Formation have a darker color relative to the host
270 rock and are systematically more fractured than the hosting limestone. High amplitude (> 1 mm),
271 bed-parallel stylolites are clearly visible in both limestones and dolostones (Fig. 5). However, in
272 some dolostones only ghosts of stylolite traces can be seen. No apparent porosity could be
273 observed in host rock limestones but the dolostones locally contain porosity, appearing as
274 millimetre- to centimetre-sized pores. Dolostone breccias in fault cores are typically clast-
275 supported, with angular and millimeter- to centimeter-sized fragments (Fig. 3C), changing to
276 crackle breccia (Woodcock and Mort, 2008) away from the main slip surface. In the proximity of
277 the main slip surface, dolostone fragments are sporadically cross-cut by millimeter-sized

278 dolomite veins. The breccia fragments, where cemented, are commonly surrounded by calcite
279 cement.

280 **4.2 Petrography**

281 **4.2.1 Early calcite cementation**

282 The early diagenetic products in the studied intervals are generally non-ferroan calcite
283 cements. The first calcite cements precipitated following a phase of bioclast micritization (*sensu*
284 Bathurst, 1975) in grain-supported intervals. In chronological order, they include: 1) fibrous
285 cements (FC) riming the bioclasts, mostly in the peloidal facies of the Calcare Massiccio
286 Formation (Fig. 6a). These cements are dark brown to non-luminescent under
287 cathodoluminescence; 2) mosaic cements (MC), commonly fill the intergranular pore spaces
288 (Fig. 6b), and also occur as syntaxial overgrowths on echinoderm fragments. They exhibit
289 deformation twinning and show a well-developed brown and orange concentrically-zoned
290 cathodoluminescence pattern (Figs. 6c and d). They contain only mono-phase all-liquid
291 inclusions. All of these cements are postdated by dolomites and high amplitude bed-parallel
292 stylolites (Fig. 6b).

293 **4.2.2 Dolomitization**

294 All the dolomite types are non-ferroan and dominantly fabric destructive. Dolomitization
295 developed in all the facies types of the Calcare Massiccio and the overlaying Bugarone
296 Formations, but only at the lower part of the Corniola Formation which consists of resedimented
297 Calcare Massiccio breccias (turbiditic lobes).

298 The two first dolomite types (D1 and D2) are the dominant dolomite types in the studied
299 outcrops. These dolomites are distributed within the damage zones of the ~ N-S and E-W
300 Jurassic rift-related extensional faults and, in places, displaced by them (Fig. 2a, site 1). The third
301 and fourth dolomite types (D3 and D4) are mainly observed within the damage zone of the
302 Montagna dei Fiori Fault (NNW-SSE), and appear only as dolomitic pockets locally replacing
303 the host rock and overgrowing D1 and D2 at the proximity of the ~ N-S and E-W extensional
304 faults. The fifth dolomite type (D5) is found only within the brecciated zones associated with the
305 Montagna dei Fiori Fault damage zone. The distinctive petrographic features of the recognized
306 dolomite types are summarized below:

307 **Dolomite 1 (D1)** is a replacive dolomite which commonly appears as dispersed rhombs and
308 aggregates, and locally rims fracture walls cemented by calcite (Figs. 6e and f). D1 postdates the
309 micritic envelopes and early calcite cements, and predates high amplitude bed- parallel stylolites
310 (Figs. 6g and h). The crystals are fine to medium sized ($< 350 \mu\text{m}$) with planar-e and planar-s
311 textures, consisting of relatively turbid, rich in host rock solid-inclusions, well-developed
312 crystals. They show red luminescence when viewed under cathodoluminescence.

313 **Dolomite 2 (D2)** is a replacive dolomite (Figs. 7a and b), infrequently occluding existing pore
314 spaces. Like D1, it also predates high amplitude bed-parallel stylolites (Figs. 6g and h). D2
315 generally exhibits a closely packed texture with no or little intercrystalline porosity. The crystals
316 are medium to coarse sized ($\leq 500 \mu\text{m}$) with planar-s to non-planar textures. They include a
317 turbid core followed by a transparent rim and trace quantities of saddle dolomite developing
318 sweeping extinction. In some crystals, one additional turbid zone rich in host rock solid
319 inclusions and fluid inclusions of mostly mono-phase is present. Cathodoluminescence
320 observations enabled to recognize the presence of D1 in their turbid cores. D2 crystals are
321 characterized by zones of bright red-pink luminescence separated by purple luminescence zones
322 (Fig. 7b).

323 **Dolomite 3 (D3)** is present as small localized bodies in the Calcare Massiccio (at the Castel
324 Manfrino reference section), in the Corniola Formation (at the Osso Caprino Road), and in the
325 Calcare Massiccio and Bugarone Formations (at the Corano Quarry) (Figs. 1b and 2a). In the
326 Corano Quarry the dolomitized Bugarone and Calcare Massiccio Formations are in the footwall
327 of the Montagna dei Fiori Fault; and juxtaposed to the undolomitized, intensely foliated Scaglia
328 Formation in the hanging wall. The SEM and BSEM analysis performed on the samples from the
329 immediate adjacent Scaglia Formation within the aforementioned fault damage zone did not
330 indicate the presence of any dolomite in this formation. Within the Bugarone Formation in this
331 fault damage zone, D3 locally cements the millimeter-sized angular breccias that are in turn
332 affected by fault-parallel stylolites (Figs. 7c and d). D3 crystals are fine to medium sized (< 300
333 μm) exhibiting planar-e to non-planar textures, with minor development of saddle morphologies
334 of larger crystals ($> 500 \mu\text{m}$) with planar-c texture (Figs. 7e to h). The replacive crystals display
335 a faint core, which compared to previous dolomite types has fewer solid inclusions. The saddle
336 crystals are occasionally replacive. They display typical curved and slightly serrated crystal
337 terminations with sweeping extinction. These saddle dolomites were only observed in the Castel

338 Manfrino reference section. D3 generally exhibit a dark purple color with bright orange zones
339 and subzones in core and/or rims when viewed under cathodoluminescence (Figs. 7e to h).

340 **Dolomite 4 (D4)** appears as a matrix replacive and dolomite cement surrounding porosity, and
341 locally replacing D1 and D2 (Figs. 8a to f). D4 also occludes bed-parallel shear fractures and
342 appears along the bed-parallel stylolites (Figs. 9a to d). In the Castel Manfrino reference section,
343 some intercrystalline vuggy porosity is filled with fine dolomite rhombs including D4 with relics
344 of D2 within their core (Figs. 8e and f). This porosity may be preserved or partially to
345 completely filled by calcite (C4). D4 crystals have a turbid, solid-inclusion rich core and
346 transparent rim. They are fine to medium sized ($< 200\text{-}350\ \mu\text{m}$), presenting planar-s and
347 infrequent non-planar textures. D4 exhibits a distinct luminescence pattern including a purple
348 zone and an irregular green subzone.

349 **Dolomite 5 (D5)** occurs as crystals cementing micro-veins that cross-cut precursor dolomite
350 types including dolomitic breccia fragments. In cemented breccias, D5 is postdated by C3. D5
351 presents a planar-c texture and is characterized by a bright red luminescence (Figs. 9e and f).

352 **4.2.3 Late calcite cementation**

353 Four generations of calcite postdating dolomitization and distributed only within the fault
354 damage zones have been identified (Figs. 10 and 11):

355 Calcite1 (C1) occurs only in Calcare Massiccio limestones and dolostones and is
356 represented as centimeter-sized veins with thickness that does not exceed 1.5 cm. It is not clear
357 whether the fracture opening and calcite precipitation was simultaneous (as shown in Ukar and
358 Laubach, 2016). These veins are strata-bound, bed-perpendicular with irregular fracture walls,
359 exhibiting white color in the outcrops. They are present within the syn-rift related extensional
360 fault damage zones, postdating the first dolomite type (D1) and abutted by high amplitude bed-
361 parallel stylolites. C1 usually shows blocky to elongated crystal morphologies and displays well-
362 developed deformation twinning planes (Type II of Burkhard, 1993). This calcite exhibits
363 concentric zonation and brown zones alternate with orange luminescence zones (Figs. 11a and
364 b).

365 Calcite 2 (C2) exclusively occurs in the intensely deformed Scaglia Formation within the
366 fault damage zones (Figs. 11b, c and d) and correspond to tension gashes associated with
367 stylolites (*sensu* Nelson, 1981). The thickness of these veins does exceed 1 cm. They are usually
368 discontinuous and branch to several microveins (thickness $< 1\text{mm}$) when their tips are not

369 intersected by stylolites. C2 veins are mostly recorded in foliated shear deformation zones with
370 well-defined S-C fabrics, exhibiting blocky, elongated to fibrous shapes with strongly developed
371 tightly spaced deformation twinning planes (Type II of Burkhard, 1993). C2 displays brown to
372 orange luminescence with locally darker sector zones. The brown to orange luminescence
373 characteristic of C2 is similar to those of encasing Scaglia host rocks (Figs. 11c and d).

374 Calcite₃ (C3) occurs as cement, filling the Montagna dei Fiori main fault plane and
375 isolated veins within its damage zone. These veins are centimeter-sized with thicknesses of less
376 than 2 cm. The breccias are generally clast-supported, but locally C3 cements the brecciated
377 fault-infillings containing angular fragments of host rock limestones, dolostones and earlier
378 calcites. In the brecciated zones, C3 always passively overgrows D5 in fractures and never cuts
379 it. C3 exhibits a translucent white color in hand specimen. The crystals are blocky with no or
380 weakly developed deformation twinning planes, and are characterized by a dark orange to brown
381 luminescence with distinct darker sector zones (Figs. 11e and f).

382 Calcite vein 4 (C4) exists as centimeter-sized isolated veins, pore-filling as well as
383 breccia cements postdating all the preceding dolomites and calcites in the Montagna dei Fiori
384 main fault plane. The breccia fragments are usually dolostones. C4 has a translucent white color
385 in hand specimen with blocky crystal morphology and no evidence of subsequent deformation
386 (e.g. deformation twinning planes), and is characterized by distinct concentric zonation (Figs.
387 11g and h).

388 **4.3 Geochemistry**

389 **4.3.1 Carbon and oxygen stable isotopes**

390 The carbon and oxygen stable isotopic data ($\delta^{13}\text{C}$ and $\delta^{18}\text{O}$) of host rocks, dolomites and
391 calcites are given in Table 1 and shown in Figures 12a and b. The marine stable isotopic
392 compositions reported by Veizer et al. (1999) were used as marine reference values.
393 Accordingly, Lower Jurassic marine limestones are characterized by $\delta^{13}\text{C}$ values of -0.5 to
394 +4.5‰ and $\delta^{18}\text{O}$ values of -2.5 to +1.0‰ V-PDB. The $\delta^{18}\text{O}$ values of the marine dolomites are
395 known to be 3-4‰ V-PDB more enriched than those of co-genetic marine limestones (Land,
396 1980; Major et al., 1992; Horita, 2014). In order to avoid data ambiguity due to physical mixing,
397 this analysis was not separately performed on early calcite cements (FC and MC). The $\delta^{13}\text{C}$ and
398 $\delta^{18}\text{O}$ values measured on bulk samples of host rock limestones. Both $\delta^{13}\text{C}$ and $\delta^{18}\text{O}$ values of the
399 host rocks are within the expected range of the Lower Jurassic marine limestones but the

400 Corniola host rocks show slightly lower values comparing to those of Calcare Massiccio. In the
401 Calcare Massiccio host rocks, the $\delta^{13}\text{C}$ values plot between +2.4 and +3.1‰ and $\delta^{18}\text{O}$ values are
402 within the range of -1.6 and 0.0‰ V-PDB. The $\delta^{13}\text{C}$ values in the Corniola host rocks are +2.0
403 and +2.5‰ while the $\delta^{18}\text{O}$ values are -3.1 to -1.4‰ V-PDB. The $\delta^{13}\text{C}$ and $\delta^{18}\text{O}$ values of the
404 Scaglia host rocks range between +1.0 to +3.3‰ for $\delta^{13}\text{C}$ and -2.2 to -1.0‰ V-PDB for $\delta^{18}\text{O}$.
405 The values obtained are characterized in the mean range of Upper Cretaceous to Paleogene
406 marine limestones (Veizer et al., 1999; +1.0 to +4.5‰ for $\delta^{13}\text{C}$ and -4.0 to +2.0‰ V-PDB for
407 $\delta^{18}\text{O}$).

408 The $\delta^{13}\text{C}$ values of C1 are between +1.6 and +2.1‰ which plot within the range of
409 reference values (Jurassic) but are slightly lower than the surrounding host rock values. The $\delta^{18}\text{O}$
410 values are between -4.7 and -2.7‰ V-PDB which are lower than those of reference and host rock
411 values.

412 The $\delta^{13}\text{C}$ values of all dolomite types (+0.6 to +3.4‰) fall within the range of host rocks
413 and Jurassic marine limestones (Veizer et al., 1999). The $\delta^{18}\text{O}$ shows a wider range of values,
414 overlapping but also lower than host rocks (-4.5 to -0.9‰ V-PDB) and those expected for the
415 Lower Jurassic marine dolomites. The majority of values plot between -3.5 and -1.5‰ V-PDB.
416 The small size and overgrowth nature of certain dolomite types (e.g. D2 and D5) limits their
417 proper isolation for geochemical analyses. Only one sample from D1 dolomite could be
418 measured for $\delta^{13}\text{C}$ and $\delta^{18}\text{O}$ values, showing +2.5 and -1.9‰ V-PDB, respectively. The $\delta^{13}\text{C}$ and
419 $\delta^{18}\text{O}$ values of D3 dolomite range from +2.0 to +2.6‰ and -2.8 to -1.9‰ V-PDB, respectively,
420 with values lower than those of the host rock.

421 D4 dolomite has $\delta^{13}\text{C}$ values between +2.4 and +2.5‰, and $\delta^{18}\text{O}$ values of -3.0 to -2.5‰
422 V-PDB. The $\delta^{13}\text{C}$ and $\delta^{18}\text{O}$ values of C2 are +1.2 to +3.1‰ and -1.7 to -1.7‰ V-PDB,
423 respectively. The $\delta^{13}\text{C}$ values of C3 are between +0.5 and +2.4‰, and the $\delta^{18}\text{O}$ values cover a
424 range of -2.2 to 0.0‰ V-PDB. The $\delta^{13}\text{C}$ and $\delta^{18}\text{O}$ values of C4 are +3.8 to +4.9‰ and -9.4
425 to -9.1‰ V-PDB, respectively. The $\delta^{13}\text{C}$ values are slightly higher but the $\delta^{18}\text{O}$ values are
426 considerably lower compared to preceding calcite generations and the measured values from host
427 rocks.

428 **4.3.2 $^{87}\text{Sr}/^{86}\text{Sr}$ ratios**

429 Samples from host rocks (i.e. Calcare Massiccio and Corniola Formations), dolomites
430 (D1, D3 and D4) and the Scaglia Formation in juxtaposition with the dolostones were analyzed

431 for their $^{87}\text{Sr}/^{86}\text{Sr}$ isotopic ratios. The obtained ratios versus $\delta^{18}\text{O}$ values of the analyzed samples
432 are shown in Fig. 12C. The $^{87}\text{Sr}/^{86}\text{Sr}$ ratios obtained from the Calcare Massiccio and Corniola
433 limestones are 0.70766 and 0.70725 ($n = 2$), respectively, which is in agreement with the values
434 of the Lower Jurassic marine carbonates (0.70704-0.70768) reported by McArthur et al. (2012).
435 CV1 show a value equal to 0.70773.

436 All the dolomite types display higher $^{87}\text{Sr}/^{86}\text{Sr}$ ratios when compared to the host rocks
437 and reference values of the Lower Jurassic marine carbonates. D1 (replacive) and D4 cements
438 show a similar narrow range with values between 0.70784 and 0.70790, respectively. The two
439 D3 samples (replacive and cement) display higher $^{87}\text{Sr}/^{86}\text{Sr}$ ratios (0.70858 and 0.70963,
440 respectively). The $^{87}\text{Sr}/^{86}\text{Sr}$ ratios obtained for dolomites do not show co-variation with
441 corresponding $\delta^{18}\text{O}$ values. The radiogenic Sr analysis was not performed on D2 and D5 since
442 the physical mixing with other dolomite types could not be avoided.

443 The $^{87}\text{Sr}/^{86}\text{Sr}$ ratios of the three marly limestone samples of Scaglia Formation are
444 0.70784 to 0.70790. The C2 veins in Scaglia Formation show similar ratios of 0.70779 and
445 0.70787. These values fit within the limits of values assigned by McArthur et al. (2012) for the
446 Cenomanian-Bartonian (Scaglia age) marine carbonates (0.70730-0.70790).

447 **4.4 Fluid inclusion microthermometry**

448 The overview of microthermometry measurements is given in Table 1 and Figs. 13A to
449 C. All the measured fluid inclusions are primary and occur in growth zones. Based on optical and
450 fluorescence microscopy analysis of wafers all the inclusions are aqueous mono-phase (liquid)
451 and two-phase (liquid and vapor) with relatively consistent L:V ratio of 10-15% within a single
452 FIA (fluid inclusion assemblage). Special care was taken to avoid the samples that occasionally
453 displayed scattered mottled luminescence that may indicate recrystallization.

454 D1 contain dominantly mono-phase aqueous inclusions with sizes greater than 5 μm . All
455 the inclusions froze at -65 to -49°C. The first melting (T_e) was detected between -22 to -19.3°C.
456 The final ice melting (T_m) appeared at temperatures between -7.7 and -2°C. Applying Bodnar's
457 (1993) equation, the obtained final melting temperatures correspond to salinity ranges of 3.5 to
458 11.3 eq. wt. % NaCl.

459 D2 is characterized by the presence of mono-phase and infrequent two-phase inclusions
460 generally within their growth zones. The homogenization temperature of two-phase inclusions
461 varies between 58 and 71°C. Upon cooling, a complete freezing of the fluid phase is reached

462 at -56 to -40°C. The first ice melting temperature was distinguished at -22°C. The final ice
463 melting temperatures fall within -17.5 and -5°C, corresponding to salinities between 7.9 and
464 20.5 eq. wt. % NaCl.

465 D3 is commonly inclusion poor. The measurable inclusions were detected and examined
466 only in saddle dolomite crystals. These crystals contain only two-phase aqueous inclusions. Their
467 homogenization temperatures are within the narrow range of 70 to 73°C. The complete freezing
468 and first ice melting temperatures could not be distinguished but the final ice melting
469 temperature occurred at temperatures between -13 and -6°C equal to salinity ranges of 9.2 to
470 16.9 eq. wt.% NaCl. The first melting temperatures of fluid inclusions in D1, D2 and D3 were
471 about -21°C, suggesting a H₂O-NaCl fluid system.

472 D4 contains only two-phase aqueous inclusions. The homogenization temperatures in D4
473 vary between 79 and 105°C. Complete freezing of inclusions occurred at temperatures
474 between -86 and -54 °C. The first ice melting was detected at -35 to -40°C indicating the
475 possible presence of divalent cations such as Ca²⁺ and/or Mg²⁺ in the fluids (Shepherd et al.,
476 1985; Goldstein and Reynolds, 1994). The final ice melting temperatures fall within a range
477 of -15 and -9°C corresponding to salinities of 12.8 to 18.6 eq. wt. % NaCl. A couple of
478 inclusions show homogenization temperatures exceeding 120°C with salinities higher than
479 20 eq. wt. % NaCl.

480 No measurable fluid inclusion could be identified in C1 and C2 due to intense
481 deformation twinning. C3 and C4 contain only primary mono-phase aqueous inclusions,
482 indicating an entrapment temperature of below about 40-50°C (Goldstein and Reynolds, 1994).
483 A complete freezing of the inclusions in C3 occurred at temperatures between -40 and -52.5°C.
484 The first melting temperature was detected at about -21 to -22°C, suggesting a H₂O-NaCl
485 composition. The final melting temperatures range between -6.4 and -2.7°C, corresponding to
486 salinities between 9.7 and 4.5 eq. wt. % NaCl. The majority of the values cluster between 7.8 and
487 5 eq. wt. % NaCl.

488 The complete freezing temperatures of the inclusions in C4 fall within -46 and -35.5°C.
489 The first melting temperature could not be determined with confidence but the final melting
490 temperatures were reached at about -0.1 to -1.8°C, corresponding to salinities of 0.17 to
491 3.0 eq. wt. % NaCl.

492 **5 Discussion**

493 **5.1 Stable and radiogenic isotopic composition of the parental fluids**

494 The $\delta^{13}\text{C}$ values of all dolomite types mimic the range of host rock and Jurassic marine
495 limestones and, consequently, they can be interpreted as largely rock-buffered. Their $\delta^{18}\text{O}$ values
496 are partly similar to those of their respective host rocks as well as Jurassic marine reference
497 values but more depleted when compared to the presumable Jurassic marine dolomites. The
498 relatively depleted $\delta^{18}\text{O}_{\text{dolomite}}$ values could indicate the contribution of heated fluids in
499 dolomitization process, although it could also relate to recrystallization of a precursor dolomite
500 by fluids at higher temperature or ^{18}O -depleted (Land, 1980; 1985). The absence of distinctive
501 textural evidence in the analyzed samples such as enlarged crystal size and/or systematic mottled
502 cathodoluminescence pattern, and their co-variation with $\delta^{18}\text{O}$ values do not confirm
503 recrystallization (Mazzullo, 1992 and ref. therein).

504 The oxygen isotope fractionation relation between water and dolomite (Land, 1983) was
505 used to determine the most plausible parental fluids. In order to avoid erroneous results due to
506 rock-buffered $\delta^{18}\text{O}$ values, only the $\delta^{18}\text{O}$ values of dolomite cements, especially from the bed-
507 parallel veins containing D4 were used. These values may provide the closest approximation to
508 the $\delta^{18}\text{O}$ signature of the parental fluids (Barker and Cox, 2011). Accordingly, a $\delta^{18}\text{O}$ value of \approx
509 +2.5 to +4‰ V-SMOW was calculated for D3, while this values increase to \approx +5 to +7.5‰
510 V-SMOW for D4 (Fig. 13d). The higher $\delta^{18}\text{O}$ composition of the dolomitizing fluids relative to
511 the Mesozoic seawater, which is estimated at -1.2 to -1‰ V-SMOW (Shackleton and Kennett,
512 1975; Marshall, 1992; Saelen et al., 1996), is compatible with fluids derived from or that had
513 interacted with siliciclastic rocks, crystalline basement (Taylor, 1997) and/or evaporite-derived
514 brines.

515 The $^{87}\text{Sr}/^{86}\text{Sr}$ ratios obtained for all dolomite types are higher than the Lower Jurassic
516 marine carbonate values (0.70704-0.70768; McArthur et al., 2012). Since marine carbonates
517 have very low rubidium (Rb) concentrations they produce negligible *in situ* radiogenic ^{87}Sr after
518 their deposition (Stueber et al. 1972; Burke et al. 1982). Therefore, the higher $^{87}\text{Sr}/^{86}\text{Sr}$ ratios can
519 be explained by the contribution of fluids originated or interacted with potassium rich
520 siliciclastic rocks (K-feldspars), crystalline basement and/or stratigraphic levels with higher
521 $^{87}\text{Sr}/^{86}\text{Sr}$ ratios (Emery and Robinson 1993; Banner, 2004). Taking into account that the Upper
522 Triassic Burano Formation underlying the studied intervals as the basal detachment has $^{87}\text{Sr}/^{86}\text{Sr}$
523 ratios between 0.70774 and 0.70794 (Boschetti et al., 2005), the $^{87}\text{Sr}/^{86}\text{Sr}$ ratios (D1 and D4) can

524 partially be explained by their contribution. However, this contribution cannot justify much
525 higher $^{87}\text{Sr}/^{86}\text{Sr}$ ratios recorded in D3, being higher than values reported for Phanerozoic
526 seawater (McArthur et al., 2012), and the values obtained for the adjacent basinal deposits (i.e.
527 Corniola and Scaglia Formations). Therefore, parental fluids most likely originated from or had
528 interacted with the siliciclastic rocks underlying the Burano Formation (Verrucano Formation), if
529 present, and/or with the crystalline basement with common elevated $^{87}\text{Sr}/^{86}\text{Sr}$ ratios (0.71500-
530 0.72650; Del Moro et al., 1982). The significantly higher $^{87}\text{Sr}/^{86}\text{Sr}$ ratios in D3 in comparison
531 with other studied dolomites indicates a higher influence of $^{87}\text{Sr}/^{86}\text{Sr}$ -rich fluids either due to
532 major changes in the permeability architecture of faults or availability of such fluids. The lack of
533 any ferroan diagenetic phase minimizes the interaction of fluids produced by clay
534 transformation/dewatering (i.e. smectite to illite transformation; Boles and Franks, 1979).

535 C1 is characterized by $\delta^{13}\text{C}$ and $\delta^{18}\text{O}$ values lower than the host limestones (i.e. Calcare
536 Massiccio), while its $^{87}\text{Sr}/^{86}\text{Sr}$ ratio is similar to them. The salinity and composition of the
537 parental fluids cannot be inferred here since no measurable fluid inclusions were found within
538 this cement. The $^{87}\text{Sr}/^{86}\text{Sr}$ ratio being within the range of the corresponding host rocks and the
539 reference values, points to a rock-buffered system for $^{87}\text{Sr}/^{86}\text{Sr}$.

540 The $\delta^{13}\text{C}$ and $\delta^{18}\text{O}$ values obtained for C2, as well as $^{87}\text{Sr}/^{86}\text{Sr}$ ratios, fall within the
541 range of the Scaglia host rocks, thus reflecting their rock-buffered nature. This interpretation is
542 further supported by the similar luminescence characteristics of C2 with that of encasing Scaglia
543 host rocks. The fluids from which C2 calcite precipitated, as expected for tension gashes, were
544 most likely derived from carbonate dissolution during pressure-solution and stylolitization of
545 host rock, pointing to a closed fluid system in contrast with the subsequent vein generations.

546 C3 is characterized by $\delta^{13}\text{C}$ values within the Jurassic marine values but are generally
547 lower than the host rocks, while their $\delta^{18}\text{O}$ values partially overlap both the hosting limestones
548 and dolostones. Microthermometry of fluid inclusions revealed only mono-phase aqueous
549 inclusions and thus precipitation at relatively low temperature ($\leq 40\text{-}50^\circ\text{C}$) with moderate
550 salinity (4.5-9.7 eq. wt. % NaCl). Such levels of salinity can be assigned to evaporated seawater,
551 residual brines or fluids derived from evaporite dissolution, and thus makes it difficult here to
552 interpret their exact origin with the available data.

553 C4 is the latest calcite phase, and records the $\delta^{13}\text{C}$ and $\delta^{18}\text{O}$ values, respectively enriched
554 and significantly depleted when compared to their hosting rocks and preceding diagenetic

555 products. Generally, the enrichment of ^{13}C could suggest CO_2 outgassing due to evaporation or
556 pressure changes (Friedman, 1970; Hendry et al., 2015) or bacterial fermentation
557 (methanogenesis) of organic matter (Hudson, 1977) in low temperature diagenetic environments.
558 The homogenization temperature of C4, being below about 40-50°C, could support any of these
559 processes. Their low $\delta^{18}\text{O}$ values and fluid inclusions with salinities similar to, but also
560 significantly lower than, seawater reflect the contribution of meteoric fluids during precipitation
561 of this calcite.

562 **5.2 Origin of the dolomitizing fluids**

563 The contribution of brines that derived from highly evaporated seawater or evaporites is
564 suggested by the elevated salinity values obtained from microthermometry of the fluid inclusions
565 (3.5 to 20.5 eq. wt. % NaCl). Accordingly, two sources that could potentially provide such fluids
566 can be proposed: 1) fluids related to the Late Messinian evaporites, associated with the overlying
567 Upper Miocene Laga Formation, and their possible downward percolation through fault zones by
568 density driven flow and/or seismic pumping mechanisms (Sibson, 1981; McCaig, 1988, 1990);
569 or their tectonic involvement into the Apenninic thrust wedge during its propagation
570 (underthrusting; Lobato et al., 1983); and 2) fluids related to the underlying detachment horizon
571 of the Burano evaporites (Upper Triassic) and their upward flow through fault zones during
572 development of the Montagna dei Fiori Anticline. The first scenario is valid if the dolomitization
573 would have occurred only from the Upper Miocene time onwards. Moreover, several researchers
574 (e.g. Vai and Ricci Lucchi, 1977; Bassetti et al., 1998; Roveri et al. 2001) have shown that the
575 occurrence of primary shallow-water evaporites, which were dominantly gypsum, was limited
576 only to the western and central parts of the northern Apennines consisting of thrust-top marginal
577 basins (Roveri et al. 2001). Hence, the evaporitic horizons existing within the Laga Formation
578 corresponds to resedimentation (gypsum debris) of those previously precipitated in the marginal
579 basins. This interpretation makes the Messinian evaporites an unlikely source of Mg-rich brines.
580 Taking into account that the maximum burial-related temperature of the Calcare Massiccio
581 Formation did not exceed 80°C in the Montagna dei Fiori region (Ronchi et al., 2003), it is
582 unlikely that the downward percolation of relatively low-temperature brines derived from the
583 Messinian evaporites, located at higher stratigraphic levels, could reach or exceed the high
584 temperatures recorded in fluid inclusions of the studied dolomites (D4; up to 105°C), given that
585 the homogenization temperatures reflect the minimum entrapment temperatures (Goldstein and

586 Reynolds, 1994). Deep circulation of these brines, if they existed, can also be excluded by the
587 fact that their limited involvement in the thrust wedge was confined merely to the off shore
588 wards of the Montagna dei Fiori region (Artoni, 2013).

589 Accordingly, the Upper Triassic Burano Formation, the basal detachment, appears as the
590 most plausible source for the high salinity brines recorded in fluid inclusions, and likewise, the
591 Mg-rich fluids could have been originated from post-evaporite brines associated with them
592 (Carpenter, 1978; McCaffrey et al., 1987). The fluctuations in salinity may argue for diverse
593 range of fault connectivity, different degrees of rock-water interaction and contribution of pore
594 waters of lower salinity (e.g. marine or meteoric).

595 **5.3 Timing and structural controls on the evolution of parental fluids**

596 A generalized paragenesis and the relative chronology of dolomitization in relation to the
597 structural evolution of the Montagna dei Fiori Anticline are illustrated in Figs. 14 and 15. The
598 structural episodes are based on the evolutionary stages of the Montagna dei Fiori Anticline
599 suggested by Storti et al. (2018). The paragenesis is constructed on the basis of direct evidences
600 recorded during observations at outcrop scale and microscopic observations (e.g. cross-cutting
601 relationships between diagenetic phases, stylolites, fractures and other structural kinematics), and
602 indirect evidences (e.g. regional geodynamics and burial history).

603 The occurrence of micritic envelopes and fibrous calcite cements (FC), in grain-
604 supported stratigraphic levels of the Calcare Massiccio Formation, is interpreted to be of
605 eogenetic origin (i.e. marine phreatic diagenesis; Moore, 1989), reflecting an early diagenesis
606 shortly after deposition. The well-developed brown and orange concentric cathodoluminescence
607 pattern of the succeeding mosaic calcite cement (MC) suggests a progressive shift to more
608 reducing conditions during precipitation in a phreatic diagenetic environment (as shown in Li et
609 al., 2017). High amplitude bed-parallel stylolites postdate both cements, which confirm their
610 precipitation before significant burial. The observations made here are in agreement with earlier
611 work by Giacometti and Ronchi (2000), interpreting that the Calcare Massiccio Formation was
612 cemented during the early diagenetic stages.

613 D1, C1 and D2 are cut by well-developed, high amplitude bed-parallel stylolites.
614 Presence of D1 and C1 in bed-perpendicular veins typically cut by these stylolites (see Figs. 6e
615 to h) support the interpretation that the first dolomitization event (D1 and D2) took place before
616 significant burial and stylolite development. The latter and bed-perpendicular veins are

617 dynamically compatible within the same stress field which is characterized by a vertical, load-
618 related maximum principal axis of the stress ellipsoid (Fig. 15a). The dominantly mono-phase
619 fluid inclusions within D1 and D2 are in agreement with precipitation temperatures below about
620 40-50°C, suggesting a relatively shallow to intermediate burial environment and hence
621 supporting a pre-Apenninic orogeny age of precipitation from a mix of formational and extra-
622 formational fluids with elevated $^{87}\text{Sr}/^{86}\text{Sr}$ ratios. The distribution of D1 and D2 localized nearby
623 the rifting-related ~ N-S and E-W striking extensional faults and even their displacement along
624 them (Fig. 2a, e.g. site 1), point to the possible contribution of these faults in occurrence of D1
625 and D2. These faults dominantly affect the Jurassic rocks older than the Maiolica Formation
626 which is attributed to post-rift deposits, therefore suggesting a pre-Maiolica age for these
627 dolomite types. Although an absolute age cannot be provided, based on the evidence discussed
628 above, the circulation of Mg-rich fluids during this dolomitization event was most likely
629 controlled by rifting-related Jurassic extensional fault zones cutting through the crystalline
630 basement. Precipitation of D1 and D2 at the lower part of Corniola Formation which is known as
631 the syn-rift deposit discards a pre-rift origin for these dolomites. The displacement of dolomites
632 along the aforementioned faults is possibly related to their prolonged activation during Early to
633 Late Jurassic. In addition to the role of these faults in channelizing the fluids, their mobilization
634 must have been intensified by some deriving mechanisms. A thermal convection system derived
635 from high heat flux during rifting was interpreted by Hollis et al. (2017) to be responsible for
636 circulation of seawater in a syn-rift dolomitization case in the Hammam Faraun fault block (Suez
637 Rift, Egypt). In such scenario, the salinity of the fluids and their $^{87}\text{Sr}/^{86}\text{Sr}$ ratios are expected to
638 be more or less within the range of seawater. Furthermore, this scenario seems unlikely in the
639 studied area given the lack of a deep aquifer to accommodate the fault tips and promotes the
640 lateral fluid flux from basin to the rift shoulders and vice versa. Taking into account that D1 and
641 D2 are the volumetrically more relevant dolomites within the studied intervals, and assuming the
642 likely role of syn-rift extensional faults (Early to Late Jurassic) in their precipitation, a
643 dominantly syn-rift dolomitization process is proposed for the dolostones in the Montagna dei
644 Fiori Anticline. Although the CL zonation pattern observed in D2 may indicate changes in flow
645 condition or fluid composition, the lack of physical disruptions such as multiple fracturing
646 suggests external regional controls rather than slip along the same faults (Eichhubl and Boles,
647 2000). The absence of pervasive syn-dolomitization fracturing and brecciation as well as zebra

648 fabrics in these dolomites, perhaps indicate a relatively calm tectonic period during dolomite
649 development (e.g. Hollis et al., 2017).

650 D3 and D4 both record elevated $^{87}\text{Sr}/^{86}\text{Sr}$ ratios which accounts for their fault-controlled
651 origin. However, their occurrence at the top of the Calcare Massiccio and overlaying Bugarone
652 Formation (Corano Quarry site) which is < 1 m thick in Montagna dei Fiori region, and is
653 marked as the final rift deposit (Cardello and Doglioni, 2015) discards a syn-rift origin for these
654 dolomites. Moreover, D3 and D4 postdate the development of high amplitude bed-parallel
655 stylolites. The formation of stylolites requires an approximate overburden of 600 to 1500 m
656 (Lind, 1993; Machel, 1999; Mountjoy et al., 1999; Schulz et al., 2016), corresponding to a late to
657 post-Maiolica deposition time (Early Cretaceous time onwards). The presence of D3 and D4
658 dolomites in bed-parallel fractures and as shear veins (D4) (Figs. 9a and b) suggests their
659 association with contractional deformations, i.e. the most likely tectonic regime for explaining
660 bed-perpendicular dilation. Therefore, the volumetrically minor second stage of dolomite
661 precipitation may possibly be related to the Late- to post-Miocene compressional tectonics
662 recorded in this region (e.g. Mazzoli et al., 2002; Artoni, 2013; Storti et al., 2018).

663 Dolostones containing D3 and D4 appear commonly as clast-supported breccias along
664 fault zones pertaining to the Montagna dei Fiori Fault, then overprinted by fault-parallel
665 stylolites (Figs. 3 and 7). Accordingly, the occurrence of these dolomites was probably
666 synchronous with the incipient stages of fault development, predating fault buttressing (Storti et
667 al., 2018). Homogenization temperatures recorded in D4 (up to 105°C), much higher than the
668 maximum temperatures recorded in the host rocks (below about 80°C; Ronchi et al., 2003),
669 suggest hydrothermal fluid circulation. The development of the Montagna dei Fiori Anticline at
670 the toe of the Late Miocene Central Apennines thrust wedge could have favored the
671 forelandward migration of hydrothermal fluids expelled from the more internal regions of the
672 belt, similarly to what has been proposed for the Rocky Mountains foreland (i.e. squeegee flow
673 model; Machel and Cavell, 1999). Such a migration may have possibly favored the precipitation
674 of D4 in bed-parallel veins, generally considered as evidence for syn-compressional fluid
675 overpressure (Sibson, 2001; Hiemstra and Goldstein, 2015). At this stage, in addition to dilation
676 of the pre-existing ~ N-S and E-W striking rift-related extensional faults and their possible role
677 in fluid migration, the excess of pore pressure at the base of the thrust ramp, in the fold hinge and
678 during fold tightening could promote the localization of the fractures (Smith and Wiltschko,

1996; Ghisetti and Vezzani, 2000), with fluid migration within this zone and eventually dolomitization. These fractures could have been corridors that later on formed the insipient NW-SE Montagna dei Fiori Fault. Their localization at the back-limb cross-cutting the core, explaining best the distribution of D3 and D4 at this locality. The presence of only D5 within the damage zone of the Montagna dei Fiori Fault, postdating dolostone brecciation and, in places, cementing breccia fragments suggest that D5 dolomite precipitation was associated with the late stage evolution of the Montagna dei Fiori Fault, predating late stage calcite precipitation. The shift from dolomite to calcite precipitation can be ascribed to attenuation of Mg-rich fluids and/or calcite saturation. This condition was perhaps initiated during the late stages of anticline evolution due to changes in fault conductivity sealing the upward migration of Mg-rich fluids. The presence of several generations of bed-perpendicular stylolites bounding and intersecting C2 veins (Fig. 10), supports the postulation that late stage calcite cements precipitated in close association with the deformation history of the Scaglia Formation in the hanging wall of the Montagna dei Fiori Fault (Fig. 3). This deformation occurred during buttressing against Calcare Massiccio and Corniola Formations in the footwall, and related with the positive inversion event induced by thrust-sheet stacking at depth (Storti et al., 2018). Precipitation of C3 and C4 is interpreted to have occurred during uplift and cooling as revealed by their relatively low homogenization temperatures ($\leq 40\text{-}50^{\circ}\text{C}$) of fluid inclusions trapped within these cements. Deformation twinning is either absent or weakly developed, reflecting the lack of significant tectonic deformation after calcite precipitation. These cements postdate the dolomitization events, high amplitude bed-perpendicular and parallel stylolites, and are precipitated as cements bounding the breccia fragments within the damage zone of the Montagna dei Fiori Fault. Salinities calculated from their fluid inclusions, particularly in C4, suggests precipitation from meteoric waters, which should have been favored during the late evolutionary stages of antiformal stacking beneath the Montagna dei Fiori Anticline, and eventual late extensional slip along the Montagna dei Fiori Fault (Storti et al., 2018). The results obtained in this study are in relative agreement with the earlier work by Ronchi et al. (2003) and Murgia et al. (2004) in the Central Apennines, assigning dolomitization phases to the pre- and syn-orogenic deformations, although they did not specify the direct relation between the local structures and the different types of dolomite.

709 The textures of the studied dolomites vary from planar-e to non-planar, the preponderance of
710 planar dolomite, as in D4, creates a rock with interesting poroperm characteristics (e.g. Woody et
711 al., 1996; Wilson et al., 2007; Wenzhi et al., 2012). This case-study is certainly relevant for
712 many potential reservoirs elsewhere in the world. Similar multistage burial dolomitization events
713 enhancing the reservoir quality have been reported from the carbonate successions of the Jurassic
714 in the Kopet-Dagh Basin, north eastern Iran (Adabi, 2009) and Devonian of the Rainbow sub-
715 Basin, western Canada (Qing and Mountjoy, 1989; Lonnee, 1999).

716 **6 Conclusions**

717 The Lower Jurassic limestones outcropping at the core of the Montagna dei Fiori
718 Anticline (Central Apennines, Italy) are massively affected by dolomitization, in damage zones
719 of the pre-orogenic faults inherited from the Tethyan rifting and the ones formed during the
720 Apenninic orogeny. Cross-cutting relationships between deformation structures, and results from
721 optical and cold cathodoluminescence petrography, fluid inclusion microthermometry, and
722 isotope geochemistry, support the occurrence of two major dolomitization events. The first event
723 is interpreted as having developed during the late stages of Tethyan rifting in Jurassic and
724 resulted in volumetrically significant dolostone geobodies. These dolostones are largely matrix
725 replacive, and their precipitation initiated prior to the significant burial as reflected in their cross-
726 cutting relationship with bed-parallel stylolites, and by homogenization temperatures in fluid
727 inclusions that are dominantly below about 40-50°C. The second dolomitization event
728 corresponds to volumetrically less relevant replacive dolomite and dolomite cements occluding
729 fractures. These dolomites precipitated during hydrothermal fluid circulation associated with
730 contractional tectonics during the Apenninic orogeny, possibly at the onset of the growth of the
731 Montagna dei Fiori Anticline (Late Miocene).

732 Dolomitizing fluids in both events were most likely sourced from evaporitic brines
733 associated to the underlying Burano evaporites and their interaction with siliciclastic rocks
734 and/or the crystalline basement.

735
736 *Author contributions.* M. Mozafari participated in fieldwork, performed petrographic and
737 microthermometric analyses, provided their interpretation, and wrote the manuscript; R.
738 Swennen participated in fieldwork, discussed the results of the diagenetic study, and critically
739 reviewed the manuscript; F. Balsamo contributed to collect and interpret structural data,

740 discussed structural diagenesis data interpretation, and critically reviewed the manuscript; H. El
741 Desouky collected $^{87}\text{Sr}/^{86}\text{Sr}$ data; F. Storti conceived the research, contributed to collect and
742 interpret structural data, discussed structural diagenesis data interpretation, and critically
743 reviewed the manuscript; C. Taberner participated in fieldwork, discussed the results of the
744 diagenetic study and their framing into the proposed structural evolution, and critically reviewed
745 the manuscript.

746
747 *Acknowledgments.* This research was performed by collaboration between Parma and KU
748 Leuven universities in the framework of a research project (PT12432 and GFSTE 1100942)
749 funded by Shell Global Solutions International (Carbonate Research Team, now Geology and
750 New Reservoir Types Team). We thank E.M. Selmo (Parma University) and M. Joachimski
751 (University of Erlangen, Germany) for the stable carbon and oxygen analysis. G. Davis (VU
752 Amsterdam, the Netherlands) is thanked for the strontium isotope analysis. A. Comelli and H.
753 Nijs are kindly thanked for the careful preparation of the wafers and thin sections. L. Barchi is
754 gratefully appreciated for his help in SEM analysis. We acknowledge A. Koopman for the
755 constructive discussions during field work. We appreciate D. Smith (Energie Beheer Nederland,
756 the Netherlands) for the careful reviewing of the manuscript. We are very grateful to reviewers J.
757 Hendry and E. Ukar for their suggestions that allowed us to significantly improve the
758 manuscript.

759

760 **References**

- 761 Adabi, M. H.: Multistage dolomitization of upper jurassic mozduran formation, Kopet-Dagh
762 Basin, NE Iran. Carbonates and Evaporites, 24, 16-32,
763 <https://doi.org/10.1007/BF03228054>, 2009.
- 764 Alvarez, W.: Evolution of the Monte Nerone Seamount in the Umbria-Marches Apennines; I,
765 Jurassic-Tertiary stratigraphy, B. Soc. Geol. Ital., 108, 3-21, 1989.
- 766 Amieux, P.: La cathodoluminescence: méthode d'étude sédimentologique des carbonates, B.
767 Cent. Rech. Explor.-Prod. Elf-Aquitaine, 6, 437-483, 1982.
- 768 Artoni, A.: Messinian events within the tectono-stratigraphic evolution of the Southern Laga
769 Basin (Central Apennines, Italy), B. Soc Geol. Ital., 122, 447-466, 2003.
- 770 Artoni, A.: The Pliocene-Pleistocene stratigraphic and tectonic evolution of the central sector of
771 the Western Periadriatic Basin of Italy, Mar. Pet. Geol., 42, 82-106,
772 <https://doi.org/10.1016/j.marpetgeo.2012.10.005>, 2013.
- 773 Banner, J. L.: Radiogenic isotopes: systematics and applications to earth surface processes and
774 chemical stratigraphy, Earth. Sci. Rev., 65, 141-194, [https://doi.org/10.1016/S0012-8252\(03\)00086-2](https://doi.org/10.1016/S0012-8252(03)00086-2), 2004.
- 775
- 776 Barchi, M., Minelli, G., and Piali G.: The CROP 03 profile: a synthesis of results of deep
777 structures of the Northern Apennines, Mem. Soc. Geol. It., 52, 383-400, 1998.
- 778 Barker, S. L., and Cox, S. F.: Evolution of fluid chemistry and fluid-flow pathways during
779 folding and faulting: an example from Taemas, NSW, Australia, Geol. Soc. London
780 Spec. Publ., 359, 203-227, <https://doi.org/10.1144/SP359.12>, 2011.
- 781 Bassetti, M. A., Ricci Lucchi, F., Roveri, M., Taviani, M.: Messinian facies in a critical section
782 of northern Apennines (Montepetra-Perticara, Pesaro), Giorn. Geol., 60, 261-263,
783 1998.
- 784 Bathurst, R. G. C. (Eds.): Carbonate sediments and their diagenesis, Dev. Sedimentol., Ser.,
785 Elsevier, 12, 658 pp., 1975.
- 786 Bathurst, R. G. C.: Deep crustal diagenesis in limestones: Revista del Instituto de Investigaciones
787 Geologicas, Deputacion Provincial, Universidad Barcelona, 34, 89-100, 1980.
- 788 Bernoulli, D., Kälin, O., and Patacca, E.: A sunken continental margin of the Mesozoic Tethys:
789 The Northern and Central Apennines, Symposium" Sédimentation jurassique W
790 Européen", Spec. Publ. Ass. Sedim. Francis, 1, 179-210, 1979.

- 791 Bodnar, R. J.: Revised equation and table for determining the freezing point depression of H₂O-
792 NaCl solutions, *Geochim. Cosmochim. Acta*, 57, 683-684, 10.1016/0016-
793 7037(93)90378-A, 1993.
- 794 Boles, J. R. and Franks, S. G.: Clay diagenesis in Wilcox Sandstone of southwest Texas:
795 Implications of smectite diagenesis and sandstone cementation, *J. Sediment. Petrol.*,
796 49, 55-70, <https://doi.org/10.1306/212F76BC-2B24-11D7-8648000102C1865D>,
797 1979.
- 798 Bollati, A., Corrado, S., and Marino, M.: Inheritance of Jurassic rifted margin architecture into
799 the Apennines Neogene mountain building: a case history from the Lucretili Mts.
800 (Latium, Central Italy), *Int. J. Earth Sci.*, 101, 1011-1031,
801 <https://doi.org/10.1007/s00531-011-0694-7>, 2012.
- 802 Bosence, D., Procter, E., Aurell, M., Kahla, A. B., Boudagher-Fadel, M., Casaglia, F., Cirilli, S.,
803 Mehdie, M., Nieto, L., Rey, J., Scherreiks, R., Soussi, M., and Waltham, D.: A
804 dominant tectonic signal in high-frequency, peritidal carbonate cycles? A regional
805 analysis of Liassic platforms from western Tethys, *J. Sediment. Res.*, 79, 389-415,
806 <https://doi.org/10.2110/jsr.2009.038>, 2009.
- 807 Boschetti, T., Venturelli, G., Toscani, L., Barbieri, M., and Mucchino, C.: The Bagni di Lucca
808 thermal waters (Tuscany, Italy): an example of CaSO₄ waters with high Na/Cl and
809 low Ca/SO₄ ratios, *J. Hydrol.*, 307, 270-293,
810 <https://doi.org/10.1016/j.jhydrol.2004.10.015>, 2005.
- 811 Brandano, M., Cornacchia, I., Raffi, I., and Tomassetti, L.: The Oligocene-Miocene stratigraphic
812 evolution of the Majella carbonate platform (Central Apennines, Italy), *Sediment.*
813 *Geol.*, 333, 1-14, <https://doi.org/10.1016/j.sedgeo.2015.12.002>, 2016.
- 814 Burke, W. H., Denison, R. E., Hetherington, E. A., Koepnick, R. B., Nelson, H. F., and Otto, J.
815 B.: Variation of seawater ⁸⁷Sr/⁸⁶Sr throughout Phanerozoic time, *Geology*, 10, 516-
816 519, [https://doi.org/10.1130/0091-7613\(1982\)10<516:VOSSTP>2.0.CO;2](https://doi.org/10.1130/0091-7613(1982)10<516:VOSSTP>2.0.CO;2), 1982.
- 817 Burkhard, M.: Calcite twins, their geometry, appearance and significance as stress-strain markers
818 and indicators of tectonic regime: a review, *J. Struct. Geol.*, 15, 351-368,
819 [https://doi.org/10.1016/0191-8141\(93\)90132-T](https://doi.org/10.1016/0191-8141(93)90132-T), 1993.
- 820 Calamita, F., Cello, G., Deiana, G., and Paltrinieri, W.: Structural styles, chronology rates of
821 deformation, and time-space relationships in the Umbria-Marche thrust system

822 (central Apennines, Italy), *Tectonics*, 13, 873-881,
823 <https://doi.org/10.1029/94TC00276>, 1994.

824 Cardello, G. L., and Doglioni, C.: From mesozoic rifting to Apennine orogeny: the gran Sasso
825 range (Italy), *Gondwana Res.*, 27, 1307-1334,
826 <https://doi.org/10.1016/j.gr.2014.09.009>, 2015.

827 Carpenter, B.: Origin and chemical evolution of brines in sedimentary basins, *Oklahoma Geol.*
828 *Surv.*, 79, 60-77, <https://doi.org/10.2118/7504-MS>, 1978.

829 Centamore, E., Chiocchini, U., and Moretti, A.. Geologia della zona tra Acerenza e Avigliano
830 (Prov. di Potenza), *Studi Geol. Camerti*, 1, 97-122,
831 <http://dx.doi.org/10.15165/studgeocam-1462>, 1971.

832 Chilovi, C., De Feyter, A. J., Minelli, G., and Barchi, M. R.. Neogene strike-slip reactivation of
833 Jurassic normal faults in the M. Nerone-M. Catria Anticline (Umbro-Marchean Apennines,
834 Italy), *Boll. Soc. Geol. It.*, 121, 199-207, 2002.

835 Choukroune, P., Gapais, D., and Merle, O.: Shear criteria and structural symmetry, *J. Struct.*
836 *Geol.*, 9, 525-530, [https://doi.org/10.1016/0191-8141\(87\)90137-4](https://doi.org/10.1016/0191-8141(87)90137-4), 1987.

837 Clemenzi, L., Storti, F., Balsamo, F., Molli, G., Ellam, R., Muchez, P., and Swennen, R.: Fluid
838 pressure cycles, variations in permeability, and weakening mechanisms along low-
839 angle normal faults: The Tellaro detachment, Italy, *Am. Assoc. Pet. Geol. Bull.*, 127,
840 1689-1710, <https://doi.org/10.1130/B31203.1>, 2015.

841 Colacicchi, R., Passeri, L., and Piali, G.: Evidences of tidal environment deposition in the
842 Calcare Massiccio formation (Central Apennines-Lower Lias), in: *Tidal Deposits*,
843 edited by: Ginsburg, R. N., Springer, Berlin, Heidelberg, Germany, 345-353,
844 <https://doi.org/10.1007/978-3-642-88494-8>, 1975.

845 Cooper, J. C., and Burbi, L.: The geology of the central Sibillini Mountains, *Mem. Soc. Geol. It.*,
846 35, 323-347, 1986.

847 Crescenti, U.: Serie stratigrafiche della serie calcarea dal Lias al Miocene nella regione
848 Marchigiana Abruzzese: parte I and II, *Mem. Soc. Geol. It.*, 8, 155-420, 1969.

849 Davies, G. R., and Smith, L. B. J.: Structurally controlled hydrothermal dolomite reservoir
850 facies: an overview, *Am. Assoc. Pet. Geol. Bull.*, 90, 1641-1690, 2006.

851 Del Moro, A., Puxeddu, M., Radicati di Brozolo, F., and Villa, I. M.: Rb-Sr and K-Ar ages of
852 minerals at temperatures of 300-400°C from deep wells in the Larderello geothermal

853 field (Italy), *Contrib. Mineral. Petr.*, 81, 349-349,
854 <https://doi.org/10.1007/BF00371688>, 1982.

855 Dewever, B., Swennen, R., and Breesch, L.: Fluid flow compartmentalization in the Sicilian fold
856 and thrust belt: implications for the regional aqueous fluid flow and oil migration
857 history, *Tectonophysics*, 591, 194-209, <https://doi.org/10.1016/j.tecto.2011.08.009>,
858 2013.

859 Dewey, J. F., Helman, M. L., Turco, E., Hutton, D. H. W., and Knott, S. D.: Kinematics of the
860 western Mediterranean, in: *Alpine Tectonics*, edited by: Coward, M. P., Dietrich, D.,
861 Park, R. G., *Geol. Soc. London Spec. Publ.*, 45, 265-283,
862 <https://doi.org/10.1144/GSL.SP.1989.045.01.15>, 1989.

863 Dewit, J., Foubert, A., El Desouky, H. A., Muchez, P., Hunt, D., Vanhaecke, F., and Swennen,
864 R.: Characteristics, genesis and parameters controlling the development of a large
865 stratabound HTD body at Matienzo (Ramales Platform, Basque-Cantabrian Basin,
866 northern Spain), *Mar. Pet. Geol.*, 55, 6-25, [10.1016/j.marpetgeo.2013.12.021](https://doi.org/10.1016/j.marpetgeo.2013.12.021), 2014.

867 Dickson, J. A. D.: Carbonate identification and genesis as revealed by staining, *J. Sediment.*
868 *Petrol.*, 36, 491-505, [https://doi.org/10.1306/74D714F6-2B21-11D7-](https://doi.org/10.1306/74D714F6-2B21-11D7-8648000102C1865D)
869 [8648000102C1865D](https://doi.org/10.1306/74D714F6-2B21-11D7-8648000102C1865D), 1966.

870 Di Francesco, L., Fabbi, S., Santantonio, M., Bigi, S., and Poblet, J.: Contribution of different
871 kinematic models and a complex Jurassic stratigraphy in the construction of a
872 forward model for the Montagna dei Fiori fault-related fold (Central Apennines,
873 Italy), *Geol. J.*, 45, 489-505, <https://doi.org/10.1002/gj.1191>, 2010.

874 Eichhubl, P., and Boles, J. R.: Rates of fluid flow in fault systems; evidence for episodic rapid
875 fluid flow in the Miocene Monterey Formation, coastal California, *Am. J. Sci.*, 300,
876 571-600, doi: [10.2475/ajs.300.7.571](https://doi.org/10.2475/ajs.300.7.571), 2000.

877 Elter, P., Giglia, G., Tongiorgi, M., and Trevisan, L.: Tensional and contractional areas in the
878 recent (Tortonian to Present) evolution of the Northern Apennines, *B. Geofis. Teor.*
879 *Appl.*, 17, 3-18, 1975.

880 Emery, D., and Robinson, A. (Eds.): *Inorganic Geochemistry: Applications to Petroleum*
881 *Geology*, Blackwell Science, Oxford, United Kingdom, 101-128, 1993.

882 Fantoni, R., and Franciosi, R.: Tectono-sedimentary setting of the Po Plain and Adriatic foreland,
883 *Rend. Lincei*, 21, 197-209, <https://doi.org/10.1007/s12210-010-0102-4>, 2010.

884 Ferraro, F., Agosta, F., Ukar, E., Grieco, D. S., Cavalcante, F., Belviso, C., and Prosser, G.:
885 Structural diagenesis of carbonate fault rocks exhumed from shallow crustal depths:
886 An example from the central-southern Apennines, Italy, *J. Struct. Geol.*, 122, 58-80,
887 <https://doi.org/10.1016/j.jsg.2019.02.008>, 2019.

888 Flecker, R., De Villiers, S., and Ellam, R. M.: Modelling the effect of evaporation on the
889 salinity- $^{87}\text{Sr}/^{86}\text{Sr}$ relationship in modern and ancient marginal-marine systems: the
890 Mediterranean Messinian Salinity Crisis, *Earth Planet. Sci. Lett.*, 203, 221-233,
891 [10.1016/S0012-821X\(02\)00848-8](https://doi.org/10.1016/S0012-821X(02)00848-8), 2002.

892 Friedman, I.: Some investigations of the deposition of travertine from Hot Springs-I. The
893 isotopic chemistry of a travertine-depositing spring, *Geochim. Cosmochim. Acta*, 34,
894 1303-1315, [https://doi.org/10.1016/0016-7037\(70\)90043-8](https://doi.org/10.1016/0016-7037(70)90043-8), 1970.

895 Gale, J. F., Laubach, S. E., Marrett, R. A., Olson, J. E., Holder, J., and Reed, R. M.: Predicting
896 and characterizing fractures in dolostone reservoirs: Using the link between
897 diagenesis and fracturing, *Geol. Soc. London Spec. Publ.*, 235, 177-192,
898 <https://doi.org/10.1144/GSL.SP.2004.235.01.08>, 2004.

899 Giacometti, A., and Ronchi, P.: Early Lias Carbonate Platform: Facies and Diagenesis Analogies
900 between the Calcare Massiccio (Umbro-Marchean Apennines) and the Inici Fm.
901 (Sicily Channel), *Mem. Soc. Geol. It.*, 55, 271-278, 2000.

902 Ghisetti, F., and Vezzani, L.: Detachments and normal faulting in the Marche fold-and-thrust belt
903 (Central Apennines, Italy): inferences on fluid migration paths, *J. Geodyn.*, 29, 345-
904 369, [https://doi.org/10.1016/S0264-3707\(99\)00057-5](https://doi.org/10.1016/S0264-3707(99)00057-5), 2000.

905 Ghisetti, F., and Vezzani, L.: Interfering paths of deformation and development of arcs in the
906 fold-and-thrust belt of the central Apennines (Italy), *Tectonics*, 16, 523-536,
907 <https://doi.org/10.1029/97TC00117>, 1997.

908 Goldstein, R. H., and Reynolds, T. J.: Systematics of Fluid Inclusions in Diagenetic Minerals,
909 *Soc. Sediment. Geol., Short Course*, 31, 199 pp., 1994.

910 Gregg, J. M.: On the formation and occurrence of saddle dolomite-discussion, *J. Sediment.*
911 *Petrol.*, 53, 1025-1033, 1983.

912 Gregg, J. M., Shelton, K. L., Johnson, A. W., Somerville, I. D., and Wright, W. R.:
913 Dolomitization of the Waulsortian limestone (lower Carboniferous) in the Irish

914 Midlands, *Sedimentology*, 48, 745-766, <https://doi.org/10.1046/j.1365->
915 3091.2001.00397.x, 2001.

916 Habermann, D., Neuser, R. D., and Richter, D. K.: REE-activated cathodoluminescence of
917 calcite and dolomite: high-resolution spectrometric analysis of CL emission (HRS-
918 CL), *Sediment. Geol.*, 101, 1-7, [https://doi.org/10.1016/0037-0738\(95\)00086-0](https://doi.org/10.1016/0037-0738(95)00086-0),
919 1996.

920 Hendry, J. P., Gregg, J. M., Shelton, K. L., Somerville, I. D., and Crowley, S. F.: Origin,
921 characteristics and distribution of fault-related and fracture-related dolomitization:
922 Insights from Mississippian carbonates, Isle of Man, *Sedimentology*, 62, 717-752,
923 <https://doi.org/10.1111/sed.12160>, 2015.

924 Hiemstra, E. J., and Goldstein, R. H.: Repeated injection of hydrothermal fluids into down-dip
925 carbonates: a diagenetic and stratigraphic mechanism for localization of reservoir
926 porosity, Indian Basin Field, New Mexico, USA, *Geol. Soc. London Spec. Publ.*,
927 406, 141-177, <https://doi.org/10.1144/SP406.1>, 2015.

928 Hollis, C., Bastesen, E., Boyce, A., Corlett, H., Gawthorpe, R., Hirani, J., Rotevatn, A., and
929 Whitaker, F.: Fault-controlled dolomitization in a rift basin. *Geology*, 45, 219-222,
930 <https://doi.org/10.1130/G38s394.1>, 2017.

931 Horita, J.: Oxygen and carbon isotope fractionation in the system dolomite-water-CO₂ to
932 elevated temperatures, *Geochim. Cosmochim. Acta*, 129, 111-124,
933 <https://doi.org/10.1016/j.gca.2013.12.027>, 2014.

934 Horvath, F.: Towards a mechanical model for the formation of the Pannonian basin,
935 *Tectonophysics*, 226, 333-357, [https://doi.org/10.1016/0040-1951\(93\)90126-5](https://doi.org/10.1016/0040-1951(93)90126-5), 1993.

936 Hudson, J. D.: Stable isotopes and limestone lithification, *Geol. Soc. London*, 133, 637-660,
937 <https://doi.org/10.1144/gsjgs.133.6.0637>, 1977.

938 Koopman, A.: Detachment tectonics in the central Apennines, Italy, Ph.D. thesis, Utrecht
939 University, The Netherlands, 155 pp., 1983.

940 Land L. S.: The isotopic and trace element geochemistry of dolomite: the state of the art, in:
941 Concepts and Models of dolomitization, edited by: Zenger D. H., Dunham J. B. and
942 Ethington R. L., *Soc. Econ. Paleontol. and Mineral., Spec. Pub.*, 28, 87-110, 1980.

943 Land L. S.: The application of stable isotopes to studies of the origin of dolomite and to
944 problems of diagenesis of clastic sediments, in: *Stable Isotopes in Sedimentary*

945 Geology, edited by: Arthur M. A., Soc. Econ. Paleontol. and Mineral, Short Course,
946 10, 4-1 , 1983.

947 Land L. S.: The origin of massive dolomite. Jour. Geol. Educ., 33, 112-125, 1985.

948 Laubach, S. E., Eichhubl, P., Hilgers, C., and Lander, R. H.: Structural diagenesis, J. Struct.
949 Geol., 32, 1866-1872, <https://doi.org/10.1016/j.jsg.2010.10.001>, 2010.

950 Li, Z., Goldstein, R. H. and Franseen, E. K.: Meteoric calcite cementation: diagenetic response to
951 relative fall in sea-level and effect on porosity and permeability, Las Negras area,
952 southeastern Spain, Sediment. Geol., 348, 1-18,
953 <https://doi.org/10.1016/j.sedgeo.2016.12.002>, 2017.

954 Lind, I. L., Berger, W. H., and Kroenke, L. W.: Stylolites in chalk from leg 130, Ontong Java
955 Plateau, in: Proceedings of the Ocean Drilling Program, scientific results, 445-451,
956 1993.

957 Lobato, L. M., Forman, J. M. A., Fazikawa, K., Fyfe, W. S., and Kerrich, R.: Uranium in
958 overthrust Archean basement, Bahia, Brazil. Canadian Mineral., 21, 647-654, 1983.

959 Lonnee, J. S.: Sedimentology, dolomitization and diagenetic fluid evolution of the Middle
960 Devonian Sulphur Point Formation, northwestern Alberta, Ph.D. thesis, University of
961 Windsor, Canada, 133 pp., 1999.

962 Luczaj, J. A., and Goldstein, R. H.: Diagenesis of the Lower Permian Krider Member, southwest
963 Kansas, USA: fluid-inclusion, U-Pb, and fission-track evidence for reflux
964 dolomitization during latest Permian time, J. Sediment. Res., 70, 762-773,
965 <https://doi.org/10.1306/2DC40936-0E47-11D7-8643000102C1865D>, 2000.

966 Machel, H. G.: Effects of groundwater flow on mineral diagenesis, with emphasis on carbonate
967 aquifers, Hydrol. J., 7, 94-107, <https://doi.org/10.1007/s100400050>, 1999.

968 Machel, H. G., Mason, R. A., Mariano, A. N., and Mucci, A.: Causes and emission of
969 luminescence in calcite and dolomite, in: Luminescence microscopy and
970 spectroscopy : Qualitative and quantitative applications, edited by: Barker, C. E., and
971 Kopp, O. C, Soc. Sediment. Geol., Short Course, 9-25, 1991.

972 Machel, H. G., and Cavell, P. A.: Low-flux, tectonically-induced squeegee fluid flow, Bull. Can.
973 Petrol. Geol., 47, 510-533, 1999.

974 Major, R. P., Lloyd, R. M. and Lucia, F. J.: Oxygen isotope composition of Holocene dolomite
975 formed in a humid hypersaline setting, *Geology*, 20, 586-588,
976 [https://doi.org/10.1130/0091-7613\(1992\)020<0586:OICOHD>2.3.CO;2](https://doi.org/10.1130/0091-7613(1992)020<0586:OICOHD>2.3.CO;2), 1992.

977 Marchegiani, L., Deiana, G., and Tondi, E.: Tettonica pre-orogena in Appennino centrale, *Stud.*
978 *Geol. Camerti*, 14, 211-228, <http://dx.doi.org/10.15165/studgeocam-807>, 1999.

979 Marino, M., and Santantonio, M.: Understanding the geological record of carbonate platform
980 drowning across rifted Tethyan margins: Examples from the Lower Jurassic of the
981 Apennines and Sicily (Italy), *Sediment. Geol.*, 225, 116-137,
982 <https://doi.org/10.1016/j.sedgeo.2010.02.002>, 2010.

983 Marshall, J. D.: Climatic and oceanographic isotopic signals from the carbonate rock record and
984 their preservation, *Geol. Mag.*, 129, 143-160,
985 <https://doi.org/10.1017/S0016756800008244>, 1992.

986 Mattei, M.: Analisi geologico-strutturale della Montagna dei Fiori (Ascoli Piceno, Italia
987 Centrale), *Geol. Romana*, 26, 327-347, 1987.

988 Mazzoli, S., Deiana, G., Galdenzi, S., and Cello, G.: Miocene fault-controlled sedimentation and
989 thrust propagation in the previously faulted external zones of the Umbria-Marche
990 Apennines, Italy, *EGU Stephan Mueller Spec. Publ. Ser.*, 1, 195-209, 2002.

991 Mazzullo, S. J.: Geochemical and neomorphic alteration of dolomite: a review, *Carbonates*
992 *Evaporites*, 7, 21-37, <https://doi.org/10.1007/BF03175390>, 1992.

993 McArthur, J. M., Howarth, R. J., and Shields, G. A.: Strontium isotope stratigraphy, in: *The*
994 *Geologic Time Scale 2012*, edited by: Gradstein, F. M., Ogg, J. G., Schmitz, M., and
995 Ogg, G., Elsevier, 127-144, <https://doi.org/10.1016/C2011-1-08249-8>, 2012.

996 McCaffrey, M. A., Lazar, B., Holland, H. D.: The evaporation path of seawater and the
997 coprecipitation of Br- and K_p with halite, *J. Sediment. Res.*, 57, 928-937,
998 <https://doi.org/10.1306/212F8CAB-2B24-11D7-8648000102C1865D>, 1987.

999 McCaig, A. M.: Deep fluid circulation in fault zones, *Geology*, 16, 867-870,
1000 [https://doi.org/10.1130/0091-7613\(1988\)016<0867:DFCIFZ>2.3.CO;2](https://doi.org/10.1130/0091-7613(1988)016<0867:DFCIFZ>2.3.CO;2), 1988.

1001 McCaig, A. M., Wickham, S. M., and Taylor, H. P.: Deep fluid circulation in alpine shear zones,
1002 Pyrenees, France: field and oxygen isotope studies, *Contrib. Mineral. Petr.*, 106, 41-
1003 60, <https://doi.org/10.1007/BF00306407>, 1990.

- 1004 Montanez, I. P.: Late diagenetic dolomitization of Lower Ordovician, upper Knox carbonates: A
1005 record of the hydrodynamic evolution of the southern Appalachian Basin, *Am.*
1006 *Assoc. Pet. Geol. Bull.*, 78, 1210-1239, 1994.
- 1007 Moore, C. H. (Eds.): Carbonate diagenesis and porosity, *Dev. Sedimentol.*, 46, Elsevier Sci.
1008 Publ., Amsterdam, The Netherlands, 338 pp., 1989.
- 1009 Morettini, E., Santantonio, M., Bartolini, A., Cecca, F., Baumgartner, P. O., and Hunziker, J. C.:
1010 Carbon isotope stratigraphy and carbonate production during the Early-Middle
1011 Jurassic: examples from the Umbria-Marche-Sabina Apennines (central Italy),
1012 *Paleog.*, *Paleocl.*, *Paleoec.*, 184, 251-273, [https://doi.org/10.1016/S0031-](https://doi.org/10.1016/S0031-0182(02)00258-4)
1013 [0182\(02\)00258-4](https://doi.org/10.1016/S0031-0182(02)00258-4), 2002.
- 1014 Mountjoy, E. W., Machel, H. G., Green, D., Duggan, J., and Williams-Jones, A. E.: Devonian
1015 matrix dolomites and deep burial carbonate cements: a comparison between the
1016 Rimbey-Meadowbrook reef trend and the deep basin of west-central Alberta, *B. Can.*
1017 *Petrol. Geol.*, 47, 487-509, 1999.
- 1018 Murgia, M. V., Ronchi, P., and Ceriani, A.: Dolomitization processes and their relationships with
1019 the evolution of an orogenic belt (Central Apennines and peri-adriatic foreland,
1020 Italy), *AAPG Hedberg series*, 1, 277-294, <https://doi.org/10.1306/1025695H13121>,
1021 2004.
- 1022 Nelson, R. A: Significance of fracture sets associated with stylolite zones, *Am. Assoc. Pet. Geol.*
1023 *Bull.*, 65, 2417-2425, 1981.
- 1024 Parotto, M., and Praturlon, A.: Geological summary of the Central Apennines, *Quad. Ric. Sci.*,
1025 90, 257-311, 1975.
- 1026 Patacca, E., Sartori, R., and Scandone, P.: Tyrrhenian basin and Apenninic arcs: Kinematic
1027 relations since late Tortonian times, *Mem. Soc. Geol. It.*, 45, 425-451,
1028 <http://hdl.handle.net/11568/11610>, 1992.
- 1029 Piali, G.: Facies di piana cotidale nel Calcarea Massiccio dell'Appennino umbro marchigiano,
1030 *Boll. Soc. Geol. It.*, 90, 481-507, 1971.
- 1031 Pierantoni, P., Deiana, G., and Galdenzi, S.: Stratigraphic and structural features of the Sibillini
1032 Mountains (Umbria-Marche Apennines, Italy), *Ital. J. Geosci.*, 132, 497-520,
1033 <https://doi.org/10.3301/IJG.2013.08>, 2013.

- 1034 Purser, B., Tucker, M. and Zenger, D.: Problems, progress and future research concerning
1035 dolomites and dolomitization, in: *Dolomites: a Volume in Honour of Dolomieu*,
1036 edited by: Purser, B., Tucker, M. and Zenger, D., IAS Spec. Publ., 21, 3-20, 1994.
- 1037 Qing, H., and Mountjoy, E. W.: Multistage dolomitization in Rainbow buildups, Middle
1038 Devonian Keg River Formation, Alberta, Canada. *J. of Sediment. Res.*, 59, 114-126,
1039 <https://doi.org/10.1306/212F8F30-2B24-11D7-8648000102C1865D>, 1989.
- 1040 Radke, B. M., and Mathis, R. L.: On the formation and occurrence of saddle dolomite, *J.*
1041 *Sediment. Res.*, 50, 1149-1168, [https://doi.org/10.1306/212F7B9E-2B24-11D7-](https://doi.org/10.1306/212F7B9E-2B24-11D7-8648000102C1865D)
1042 [8648000102C1865D](https://doi.org/10.1306/212F7B9E-2B24-11D7-8648000102C1865D), 1980.
- 1043 Ronchi, P., Casaglia, F., and Ceriani, A.: The multiphase dolomitization of the Liassic Calcare
1044 Massiccio and Corniola successions (Montagna dei Fiori, Northern Apennines, Italy),
1045 *Boll. Soc. Geol. It.*, 122, 157-172, 2003.
- 1046 Rosenbaum, J., and Sheppard, S. M.: An isotopic study of siderites, dolomites, and ankerites at
1047 high temperatures, *Geochim. Cosmochim. Acta*, 50, 1147-1150,
1048 [https://doi.org/10.1016/0016-7037\(86\)90396-0](https://doi.org/10.1016/0016-7037(86)90396-0), 1986.
- 1049 Roveri, M., Bassetti, M. A., and Lucchi, F. R.: The Mediterranean Messinian salinity crisis: an
1050 Apennine foredeep perspective, *Sediment. Geol.*, 140, 201-214,
1051 [https://doi.org/10.1016/S0037-0738\(00\)00183-4](https://doi.org/10.1016/S0037-0738(00)00183-4), 2001.
- 1052 Saelen, G., Doyle, P., and Talbot, M. R.: Stable-isotope analyses of belemnite rostra from the
1053 Whitby Mudstone Fm., England: Surface water conditions during deposition of a
1054 marine black shale, *Palaios*, 11, 97-117, <https://doi.org/10.2307/3515065>, 1996.
- 1055 Santantonio, M., and Carminati, E.: Jurassic rifting evolution of the Apennines and Southern Alps
1056 (Italy): Parallels and differences, *Geol. Soc. Am. B.*, 123, 464-484,
1057 <https://doi.org/10.1130/B30104.1>, 2011.
- 1058 Santantonio, M. and Muraro, C.: The Sabina Plateau, Palaeoescrapment, and Basin-Central
1059 Apennines, 6th international symposium on the Jurassic system, General Field Trip
1060 Guidebook, Palermo, Italy, 271-315, 2002.
- 1061 Santantonio, M., Fabbi, S., and Bigi, S.: Discussion on «Geological map of the partially
1062 dolomitized Jurassic succession exposed in the central sector of the Montagna dei
1063 Fiori Anticline, Central Apennines, Italy», *Ital. J. Geosci.*, 136, 312-316,
1064 <https://doi.org/10.3301/IJG.2017.04>, 2017.

- 1065 Schulz, H. M., Wirth, R., and Schreiber, A.: Organic-inorganic rock-fluid interactions in
1066 stylolitic micro-environments of carbonate rocks: a FIB-TEM study combined with a
1067 hydrogeochemical modelling approach, *Geofluids*, 16, 909-924,
1068 <https://doi.org/10.1111/gfl.12195>, 2016.
- 1069 Scisciani V., Tavarnelli, E., and Calamita, F.: The interaction of extensional and contractional
1070 deformations in the outer zones of the Central Apennines, Italy, *J. Struct. Geol.*, 24,
1071 1647-1658, [https://doi.org/10.1016/S0191-8141\(01\)00164-X](https://doi.org/10.1016/S0191-8141(01)00164-X), 2002.
- 1072 Shackleton, N. J., and Kennett, J. P.: Paleotemperature History of the Cenozoic and the Initiation
1073 of Antarctic Glaciation Oxygen and Carbon Isotope Analyses in DSDP Sites 277, 279,
1074 and 281, Initial reports of Deep Sea Drilling Project, 29, 743-755, 1975.
- 1075 Sharp, I., Gillespie, P., Morsalnezhad, D., Taberner, C., Karpuz, R., Vergés, J., Horbury, A.,
1076 Pickard, N., J. Garland, J., and Hunt, D.: Stratigraphic architecture and fracture-
1077 controlled dolomitization of the Cretaceous Khami and Bangestan groups: an outcrop
1078 case study, Zagros Mountains, Iran, *Geol. Soc. London Spec. Publ.*, 329, 343-396,
1079 <https://doi.org/10.1144/SP329.14>, 2010.
- 1080 Shepherd, T., Rankin, A. H., and Alderton, D. H. M. (Eds.): *A Practical Guide to Fluid Inclusion*
1081 *Studies*, Glasgow: Blackie, 239 pp., 1985.
- 1082 Sibley, D. F., and Gregg, J. M.: Classification of dolomite rock textures, *J. Sediment. Petrol.*, 57,
1083 967-975, <https://doi.org/10.1306/212F8CBA-2B24-11D7-8648000102C1865D>,
1084 1987.
- 1085 Sibson, R. H.: Fluid flow accompanying faulting: field evidence and models, *Earthquake*
1086 *prediction: an international review*, AGU, 4, 593-603,
1087 <https://doi.org/10.1029/ME004p0593>, 1981.
- 1088 Slobodník, M., Mucchez, P., Kral, J., and Keppens, E.: Variscan veins: record of fluid circulation
1089 and Variscan tectonothermal events in Upper Palaeozoic limestones of the Moravian
1090 Karst, Czech Republic, *Geol. Mag.*, 143, 491-508,
1091 <https://doi.org/10.1017/S0016756806001981>, 2006.
- 1092 Smith, R. E., Wiltschko, D. V.: Generation and maintenance of abnormal fluid pressures beneath
1093 a ramping thrust sheet: isotropic permeability experiments, *J. Struct. Geol.*, 18, 951-
1094 970, [https://doi.org/10.1016/0191-8141\(96\)00023-5](https://doi.org/10.1016/0191-8141(96)00023-5), 1996.

- 1095 Steiger, R., and Jäger, E.: Subcommission on geochronology: convention on the use of decay
1096 constants in geo and cosmo chronology, *Earth Planet. Sci. Lett.*, 36, 359-362,
1097 [https://doi.org/10.1016/0012-821X\(77\)90060-7](https://doi.org/10.1016/0012-821X(77)90060-7), 1977.
- 1098 Storti, F., Balsamo, F., and Koopman, A.: Geological map of the partially dolomitized Jurassic
1099 succession exposed in the core of the Montagna dei Fiori Anticline, Central
1100 Apennines, Italy, *Ital. J. Geosci.*, 136, 125-135, <https://doi.org/10.3301/IJG.2016.05>,
1101 2017a.
- 1102 Storti F., Balsamo, F., and Koopman, A.: Reply to: discussion on «Geological map of the
1103 partially dolomitized Jurassic succession exposed in the central sector of the
1104 Montagna dei Fiori Anticline, Central Apennines, Italy» by Santantonio, M., Fabbi,
1105 S. and Bigi, S., *Ital. J. Geosci.*, 136, 317-319, <https://doi.org/10.3301/IJG.2017.04>,
1106 2017b.
- 1107 Storti, F., Balsamo F., Mozafari M., Koopman A., Swennen R. and Taberner C.: Syn-
1108 contractional overprinting between extension and shortening along the Montagna dei
1109 Fiori Fault during Plio-Pleistocene antiformal stacking at the Central Apennines
1110 thrust wedge toe, *Tectonics*, <https://doi.org/10.1029/2018TC005072>, 2018.
- 1111 Stueber, A. M., Pushkar, P., and Baldwin, A. D., JR.: Survey of $^{87}\text{Sr}/^{86}\text{Sr}$ ratios and total
1112 strontium concentrations in Ohio stream and ground waters, *Ohio J. Sci.*, 72, 98-104,
1113 1972.
- 1114 Sommer, S. E.: Cathodoluminescence of carbonates, 1. Characterization of cathodoluminescence
1115 from carbonate solid solutions, *Chemical Geology*, 9, 257-273,
1116 [https://doi.org/10.1016/0009-2541\(72\)90064-2](https://doi.org/10.1016/0009-2541(72)90064-2), 1972.
- 1117 Swennen, R., Dewit, J., Fierens, E., Muchez, Ph., Shah, M., Nader, F. H., Hunt, D.: Multiple
1118 dolomitisation events along the Ranero fault (Pozalagua Quarry, Basque-Cantabrian
1119 Basin): episodic earthquake activity, *Sedimentology*, 59, 1345-1374,
1120 <https://doi.org/10.1111/j.1365-3091.2011.01309.x>, 2012.
- 1121 Tavani, S., Storti, F., Salvini, F., and Toscano, C.: Stratigraphic versus structural control on the
1122 deformation pattern associated with the evolution of the Mt. Catria anticline, Italy, *J.*
1123 *Struct. Geol.*, 30, 664-681, <https://doi.org/10.1016/j.jsg.2008.01.011>, 2008.

- 1124 Taylor, H. P.: Oxygen and hydrogen isotope relationships in hydrothermal mineral deposits, In:
1125 Geochemistry of hydrothermal ore deposits, edited by: Barnes, H. L., Wiley and
1126 Sons, New York, 229-302, 1997.
- 1127 Thirlwall, M. F.: Long-term reproducibility of multicollector Sr and Nd isotope ratio analysis,
1128 Chemical Geology, 94, 85-104, [https://doi.org/10.1016/S0009-2541\(10\)80021-X](https://doi.org/10.1016/S0009-2541(10)80021-X),
1129 1991.
- 1130 Tongiorgi, M., Rau, A., and Martini, I. P.: Sedimentology of early-alpine, fluvio-marine, clastic
1131 deposits (Verrucano, Triassic) in the Monti Pisani (Italy), Sediment. Geol., 17, 311-
1132 332, [https://doi.org/10.1016/0037-0738\(77\)90051-3](https://doi.org/10.1016/0037-0738(77)90051-3), 1977.
- 1133 Ukar, E., and Laubach, S. E.: Syn- and postkinematic cement textures in fractured carbonate
1134 rocks: Insights from advanced cathodoluminescence imaging, Tectonophysics, 690,
1135 190-205, <https://doi.org/10.1016/j.tecto.2016.05.001>, 2016.
- 1136 Vai, G. B., and Ricci Lucchi, F.: Algal crusts, autochthonous and clastic gypsum in a
1137 cannibalistic evaporite basin: a case history from the Messinian of northern
1138 Apennines. Sedimentology, 24, 221-244, [https://doi.org/10.1111/j.1365-
1139 3091.1977.tb00255.x](https://doi.org/10.1111/j.1365-3091.1977.tb00255.x), 1977.
- 1140 Vandeginste, V., Swennen, R., Gleeson, S. A., Ellam, R. M., Osadetz, K., and Roure, F.: Zebra
1141 dolomitization as a result of focused fluid flow in the Rocky Mountains Fold and
1142 Thrust Belt, Canada. Sedimentology, 52, 1067-1095, [https://doi.org/10.1111/j.1365-
1143 3091.2005.00724.x](https://doi.org/10.1111/j.1365-3091.2005.00724.x), 2005.
- 1144 Vandeginste, V., Swennen, R., Gleeson, S. A., Ellam, R. M., Osadetz, K., and Roure, F.:
1145 Geochemical constraints on the origin of the Kicking Horse and Monarch Mississippi
1146 Valley-type lead-zinc ore deposits, southeast British Columbia, Canada, Mineralium
1147 Deposita, 42, 913-935, <https://doi.org/10.1007/s00126-007-0142-6>, 2007.
- 1148 Veizer, J., Ala, D., Azmy, K., Bruckshen, P., Buhl, D., Bruhn, F., Carden, G. A. F., Diener, A.,
1149 Ebner, S., Godderis, Y., Jasper, T., Korte, C., Pawellek, F., Podlaha, O. G., and
1150 Strauss, H.: $^{87}\text{Sr}/^{86}\text{Sr}$, $\delta^{13}\text{C}$ and evolution of Phanerozoic seawater, Chemical
1151 Geology, 161, 59-88, [https://doi.org/10.1016/S0009-2541\(99\)00081-9](https://doi.org/10.1016/S0009-2541(99)00081-9), 1999.
- 1152 Walker, G., Abumere, O. E., and Kamaluddin, B.: Luminescence spectroscopy of Mn²⁺ rock-
1153 forming carbonates, Mineral. Mag., 53, 201-11, [10.1180/minmag.1989.053.370.07](https://doi.org/10.1180/minmag.1989.053.370.07),
1154 1989.

1155 Wenzhi, Z., Anjiang, S., Suyun, H., Baomin, Z., Wenqing, P., Jingao, Z. and Zecheng, W.: Geological
1156 conditions and distributional features of large-scale carbonate reservoirs onshore China.
1157 *Petrol. Explor. Develop.*, 39, 1-14, [https://doi.org/10.1016/S1876-3804\(12\)60010-X](https://doi.org/10.1016/S1876-3804(12)60010-X), 2012.

1158 Wilson, A., and Ruppel, C.: Salt tectonics and shallow subsea floor fluid convection: models of
1159 coupled fluid-heat-salt transport, *Geofluids*, 7, 377-386,
1160 <https://doi.org/10.1111/j.1468-8123.2007.00191.x>, 2007.

1161 Wilson, M. E. J., Evans, M. J., Oxtoby, N. H., Nas, D. S., Donnelly, T. and Thirlwall, M.:
1162 Reservoir quality, textural evolution, and origin of fault-associated dolomites. *AAPB*
1163 *Bull.*, 91, 1247-1272, 2007.

1164 Woodcock, N. H., and Mort, K.: Classification of fault breccias and related fault rocks, *Geol.*
1165 *Mag.*, 145, 435-440, <https://doi.org/10.1017/S0016756808004883>, 2008.

1166 Woody, R. E., Gregg, J. M. and Koederitz, L. F.: Effect of texture on petrophysical properties of
1167 dolomite: Evidence from the Cambrian-Ordovician of Southeastern Missouri. *AAPG*
1168 *Bull.*, 80, 119-131, 1996.

1169 Zempolich, W. G., and Hardie, L. A.: Geometry of dolomite bodies within deep-water
1170 resedimented oolite of the Middle Jurassic Vajont Limestone, Venetian Alps, Italy:
1171 Analogs for hydrocarbon reservoirs created through fault-related burial
1172 dolomitization, in: *Reservoir quality prediction in sandstones and carbonates*, edited
1173 by: Kupecz, A., Gluyas, J., and Bloch, S., *AAPG Mem.*, 69, 127-162, 1997.

1174

1175

1176

1177

1178

1179

1180

1181

1182 **Table captions**

1183 **Table. 1.** Stable carbon and oxygen isotopes, $^{87}\text{Sr}/^{86}\text{Sr}$ ratios, and fluid inclusion
1184 microthermometry data (not pressure corrected) of host rocks and diagenetic phases in the
1185 Montagna dei Fiori Anticline. Stable carbon and oxygen isotopes values are expressed in
1186 ‰ V-PDB and salinity values in eq. wt. % NaCl.

1187 **Figure captions**

1188 Fig. 1. a) Simplified regional map (modified after Ghisetti and Vezzani, 1997) showing the
1189 tectonic outlines of the Central Apennines and the study area (rectangle). b) Schematic
1190 geological map of the Montagna dei Fiori Anticline showing the distribution of dolostones
1191 (modified after Storti et al., 2017a). c) Lithostratigraphical column of the successions exposed in
1192 Montagna dei Fiori (modified after Mattei, 1987; Di Francesco et al, 2010; Storti et al., 2018).
1193 Letter *B* stands for the Bugarone Formation. Lithologies are mentioned in the text. Note that the
1194 thickness of the not-outcropping formations (Triassic evaporites and the crystalline basement) is
1195 not to scale. d) Regional geological transect across present day Central Apennines and the
1196 Adriatic Sea (modified after Fantoni and Franciosi, 2010) with vertical exaggeration of 2:1. The
1197 dashed rectangle indicates the Montagna dei Fiori Anticline region.

1198
1199 Fig. 2. a, b) Geological map of the central sector of the Montagna dei Fiori Anticline, and cross-
1200 section oriented parallel (a-b) to the hinge line representing the tectono-stratigraphic architecture
1201 of the faulted anticline (modified after Storti et al., 2017a). The stereonet (Schmidt equal area
1202 projection lower hemisphere) provide the attitude of the extensional faults. The locations of the
1203 corresponding field sites are indicated by letters. c) At this location, well exposed N-S striking
1204 extensional fault zones offset the dolomitized Corniola Formation. The fault zone is
1205 characterized by near-horizontal stylolites localized in the footwall damage zone (4 fault data). d,
1206 e and f) These locations consist of mostly ~ E-W striking extensional fault zones. Particularly the
1207 boundary fault zones delimiting Calcare Massiccio Formation in the main horst block is evident
1208 (site d: 20 fault data; site e: 24 fault data; site f: 9 fault data). g and h) At these locations, dip-slip
1209 slickenlines support major extensional movements related to the Montagna dei Fiori Fault.
1210 Contractional deformation structures are preserved in the bed-perpendicular stylolites, shear
1211 surfaces and tension gashes arranged as S-C arrays (site g: 21 fault data; site h: 14 fault data).
1212 Equal area projection, lower hemisphere.

1213
1214 Fig. 3. a) Field photograph showing the deformed Scaglia Formation in the hanging wall (HW)
1215 and brecciated, dolomitized Calcare Massiccio Formation in the footwall (FW) of the Montagna
1216 dei Fiori Fault. The red arrow indicates the sense of fault movement. b) A hand specimen from
1217 the deformed Scaglia formation showing abundant pressure solution seams (TS), indicated by
1218 arrows, cross-cutting calcite veins (C2). c) A transmitted light photomicrograph of the
1219 dolomitized, brecciated Calcare Massiccio Formation. Note all the breccia fragments are
1220 composed of dolomite (D4 here).

1221
1222 Fig. 4. Field photographs (Corano Quarry) showing the field relations between dolostones (only
1223 D3 here), host limestones and the Montagna dei Fiori Fault: a) Panoramic view showing the
1224 spatial relationship between limestones and dolostones (orange) in the damage zone of the
1225 Montagna dei Fiori Fault (F). Note that the limestones and including dolostones of the Calcare
1226 Massiccio and Bugarone Formations on the footwall (FW) and marly limestones of the Scaglia
1227 Formation on the hangingwall (HW) are intensely deformed. b) Plan view of the dolomitized
1228 Calcare Massiccio limestone in the footwall damage zone: intersected by calcite veins (C1)
1229 which are partially dolomitized, and affected by bed-perpendicular stylolites (arrows). c) Distinct
1230 transition (dashed line) between dolomitized and undolomitized Calcare Massiccio limestone in
1231 the footwall damage zone.

1232
1233 Fig. 5. Field photograph (a) and a simplified sketch (b) in field site d showing a dolomitic pocket
1234 (grey color) and its relation with bed-parallel stylolites within the Calcare Massiccio Formation
1235 (hammer is 40 cm long). Note C1 is the only calcite cement here.

1236
1237 Fig. 6. Undolomitized and dolomitized Calcare Massiccio Formation in field site d: a)
1238 Transmitted light image showing a micritic peloid rimmed by fibrous cements (FC) which are
1239 overgrown by mosaic cements (MC). b) Transmitted light image showing mosaic cements (MC)
1240 in a peloidal limestone overprinted by high amplitude bed-parallel stylolites (dotted white line).
1241 Note the core of some of the peloids is partially cemented as well. c, d) Respectively, transmitted
1242 light and corresponding cathodoluminescence image of FC and MC cements. e) Transmitted
1243 light photomicrograph showing D1 crystals (arrows) lining a fracture which is cemented by C1.

1244 The fracture is in turn affected by a bed-parallel stylolite. f) Cathodoluminescence image
1245 showing D1 scattered in the host rock and riming the fracture. g, h) Respectively, transmitted
1246 light and corresponding cathodoluminescence image showing part of a bed-parallel stylolite
1247 (dotted white line) overprinting D1 and D2 crystals.

1248

1249 Fig. 7. a, b) Photomicrographs of respectively, transmitted light and corresponding
1250 cathodoluminescence image showing the zoned rhombs of D2 with the remnants of D1 preserved
1251 in their cloudy core sampled from dolomitized Calcare Massiccio Formation in field site d. The
1252 pore space is occluded by D4. c, d) D3 cementing angular breccia fragments of the Bugarone
1253 Formation in the damage zone of the Montagna dei Fiori Fault in the Corano Quarry site. Note
1254 the breccia is overprinted by a fault-parallel bed-perpendicular stylolite. e, f) Photomicrographs
1255 of respectively, transmitted light and corresponding cathodoluminescence image showing the
1256 euhedral to subhedral crystals of D3 entirely replacing the matrix and also present as cement
1257 developing a bright subzone and rim sampled from dolomitized Corniola Formation in Osso-
1258 caprino road. g, h) D3 with a saddle crystal outline (SD) postdating calcite cements (MC) and a
1259 zoned D2 crystal. The saddle morphology is outlined by a dotted white line.

1260

1261 Fig. 8. Photomicrographs of respectively, transmitted light and corresponding
1262 cathodoluminescence image of dolomite types: a, b) The cross-cutting relationship between D3
1263 and D4 sampled from dolomitized Corniola Formation in Osso-caprino road. Note the presence
1264 of D3 within the core of dolomite crystals overgrown by D4. c, d) Successions of dolomite types
1265 sampled from dolomitized Calcare Massiccio Formation in field site f. Note the green CL color
1266 of D4 crystals. Typically, luminescent dolomites are known to show yellow, orange to red colors
1267 (Machel et al., 1991). Green luminescence in carbonates including dolomite have been attributed
1268 by a number of researchers to the incorporation of three valent rare earth elements (REE) such as
1269 Dy^{3+} and U^{3+} as luminescence activators within their crystal lattice (Luczaj and Goldstein, 2000).
1270 Another possibility is the emplacement of Mn^{2+} , with yellow luminescence, in Ca^{2+} sites with
1271 blue luminescence in the dolomite crystal lattice instead of preferential incorporation in the Mg^{2+}
1272 site (Sommer, 1972b; Amieux, 1982; Walker et al., 1989; Habermann et al., 1999). Accordingly,
1273 non-stoichiometric, Ca-rich and poorly ordered dolomites may favor Mn^{2+} incorporation into

1274 their Ca²⁺ site. e, f) Vuggy porosity rimmed by D4 (green CL). Note the porosity is filled with
1275 fine dolomite rhombs including traces of D2 in their core and D4 overgrowths.

1276

1277 Fig. 9. Photomicrographs showing respectively, transmitted light and corresponding
1278 cathodoluminescence image of D4 and D5 in relation to stylolites and fracturing: a, b) D4,
1279 exploiting a bed-parallel stylolite that crossed-cuts D1 and D2 sampled from dolomitized Calcare
1280 Massiccio Formation in field site d. c, d) A sub-horizontal fracture cemented by D4 sampled
1281 from dolomitized Corniola Formation in field site f. e, f) D5 microveins (arrows) intersecting all
1282 the predating dolomite types in the footwall brecciated zone of the Montagna dei Fiori Fault,
1283 sampled from dolomitized Calcare Massiccio Formation in Castel Manfrino site.

1284

1285 Fig. 10. Field photographs showing the major calcite vein settings observed in Montagna dei
1286 Fiori: a) Cross-sectional view of bed normal Calcite vein 1 (C1) abutting bed-parallel stylolites
1287 in folded beds of the Calcare Massiccio Formation. b) Plan view of the Calcite vein 2 (C2)
1288 intensely affecting the deformed Scaglia (Rossa) Formation. c, d) Cross-sectional view of the
1289 Scaglia Formation, intensely affected by pressure solution seams of tectonic origin crossed-over
1290 by populations of bed-perpendicular Calcite veins (C3) in en echelon extensional arrays.

1291

1292 Fig. 11. a) Cathodoluminescence and transmitted light (in set) image showing blocky to
1293 elongated crystals of C1 with zoned CL pattern in the Corano Quarry site. b) Transmitted light
1294 image showing intensely twinned C1 crystals overprinted by euhedral to subhedral crystals of D3
1295 in the Corano Quarry site. Photomicrographs of respectively, transmitted light and corresponding
1296 cathodoluminescence image: c, d) C2 in the Scaglia Formation abutted by a bed-perpendicular
1297 stylolite (indicated by white arrows and dashed line) in the Corano Quarry site. The crystals
1298 display blocky to fibrous morphologies, deformation twinning, and a similar orange
1299 luminescence pattern similar to the adjacent host rock. e, f) C3 cementing the breccia fragments
1300 in the damage zone of the Montagna dei Fiori Fault. The crystals are blocky and show faint
1301 deformation twinning. They are brown-orange with distinct darker luminescence sector zones. g,
1302 h) C4 present as a cement within a polygonal pore space rimmed by dolomite, sampled from
1303 dolomitized Calcare Massiccio Formation in field site f. Note the blocky crystals, absence of

1304 deformation twinning and distinct concentric luminescence zonation pattern. C4 is corroded and
1305 followed by a late telogenetic calcite.

1306
1307 Fig. 12. Overview of the $\delta^{13}\text{C}$ and $\delta^{18}\text{O}$ values of dolomites (a) host rocks from Montagna dei
1308 Fiori as well as calcite veins (b). The stable isotope value of Lower Jurassic marine limestones
1309 based on Veizer et al. (1999) is indicated by a dashed rectangle in subset B. The $\delta^{18}\text{O}$ values of
1310 the marine dolomites are considered to be 3-4‰ V-PDB higher than those of marine limestones
1311 (Land, 1980; Major et al., 1992; Horita, 2014). c) Cross-plot of $^{87}\text{Sr}/^{86}\text{Sr}$ ratios and
1312 corresponding $\delta^{18}\text{O}$ values of host rocks, dolomites and calcite veins compared with Lower
1313 Jurassic marine carbonates $^{87}\text{Sr}/^{86}\text{Sr}$ (dashed rectangle) framework reported by McArthur et al.
1314 (2012).

1315
1316 Fig. 13. Overview of microthermometry analysis of primary inclusions in Montagna dei Fiori: a)
1317 Frequency distribution of the $T_{m_{ice}}$ (°C) in dolomite types. b) Frequency distribution of the
1318 T_h (°C) in dolomite types. c) Salinity (eq. wt. % NaCl) versus T_h (°C) of dolomite and calcite
1319 phases. d) Isotopic fractionation diagram from Land (1983) used to determine the isotopic
1320 composition (‰ V-SMOW) of parental fluids in equilibrium with dolomites in Montagna dei
1321 Fiori.

1322
1323 Fig. 14. Generalized paragenesis of diagenetic phases in relation to deformational stages and
1324 burial history of the Calcare Massiccio Formation in the Montagna dei Fiori Anticline. The
1325 deformational stages are from Storti et al. (2018), and the burial curve is based on Ronchi et al.
1326 (2003). The burial curve was made based on paleo-depth, paleo-temperatures, sedimentation rate
1327 and paleo-heat flow.

1328
1329 Fig. 15. Sketch showing the successive fault-related diagenetic phases, of most importantly
1330 dolomitization, recorded in the carbonate succession exposed at the core of the Montagna dei
1331 Fiori Anticline (not scaled). Different diagenetic phases are indicated with different colors. a)
1332 The first dolomitization event is pre-orogenic (syn-rift), triggered from the fluids channelized
1333 along Jurassic ~ E-W and ~ N-S striking extensional faults. This event occurred during burial
1334 compaction and development of bed-parallel stylolites (BS). It is represented by scattered

1335 dolomite rhombs (D1) followed by calcite cementation (C1). The dolomitization continued with
1336 precipitation of larger crystals of D2. b) Second dolomitization event: syn-orogenic (early
1337 folding/ faulting) dolomitization from fluids that migrated from more internal regions of the
1338 thrust belt and were channelized along the basal detachment level into the fold core. This
1339 dolomitization event presents matrix replacive and cements displaying infrequent saddle outlines
1340 (SD) in pore spaces, within bed-parallel veins and shear fractures. These dolostones postdate
1341 compaction but are affected by bed-perpendicular stylolites (TS) generated by horizontal to sub-
1342 horizontal layer-parallel shortening related to the growth of the Montagna dei Fiori Anticline. c)
1343 Extensional collapse of the anticline and development of the Montagna dei Fiori Fault, followed
1344 by buttressing of the Scaglia against Calcare Massiccio and Corniola Formations during positive
1345 inversion induced by continuing underthrusting at depth. Precipitation of D5 in micro-veins and
1346 cements in breccia zones, followed by late stage calcite cementation in the Montagna dei Fiori
1347 Fault damage zone (C2, C3 and C4).

	Stable isotopes		Sr isotopes	Fluid inclusion microthermometry		
	$\delta^{13}\text{C}$	$\delta^{18}\text{O}$	$^{87}\text{Sr}/^{86}\text{Sr}$	Th ($^{\circ}\text{C}$)	Salinity	n
Calcare Massiccio Fm.	+2.4 to +3.1	-1.6 to 0.0	0.70766	-	-	
Corniola Fm.	+2.0 to +2.5	-3.1 to -1.4	0.70725	-	-	
Scaglia Fm.	+1.0 to +3.1	-2.2 to -1.0	0.70784-0.70791	-	-	
D1	+2.5	-1.9	0.70789	$\leq 40-50$	3.5 to 11.3	27
CV1	+1.6 to +2.1	-4.7 to -2.7	0.70773	-	-	-
D2	-	-	-	$\leq 40-50$ to 71	7.9 to 20.5	37
D3	+2.0 to +2.6	-2.8 to -1.9	0.70859-0.70964	70 to 73	9.2 to 16.9	9
D4	+2.4 to +2.5	-3.0 to -2.5	0.70790	79 to 105	12.8 to 18.6	7
CV2	+1.2 to +3.1	-1.7 to -1.6	0.70779 - 0.70787	-	-	
CV3	+0.5 to +2.4	-2.2 to 0.0	-	$\leq 40-50$	4.5 to 9.7	9
CV4	+3.8 to +4.9	-9.4 to -9.1	-	$\leq 40-50$	0.17 to 3.0	19

Table. 1

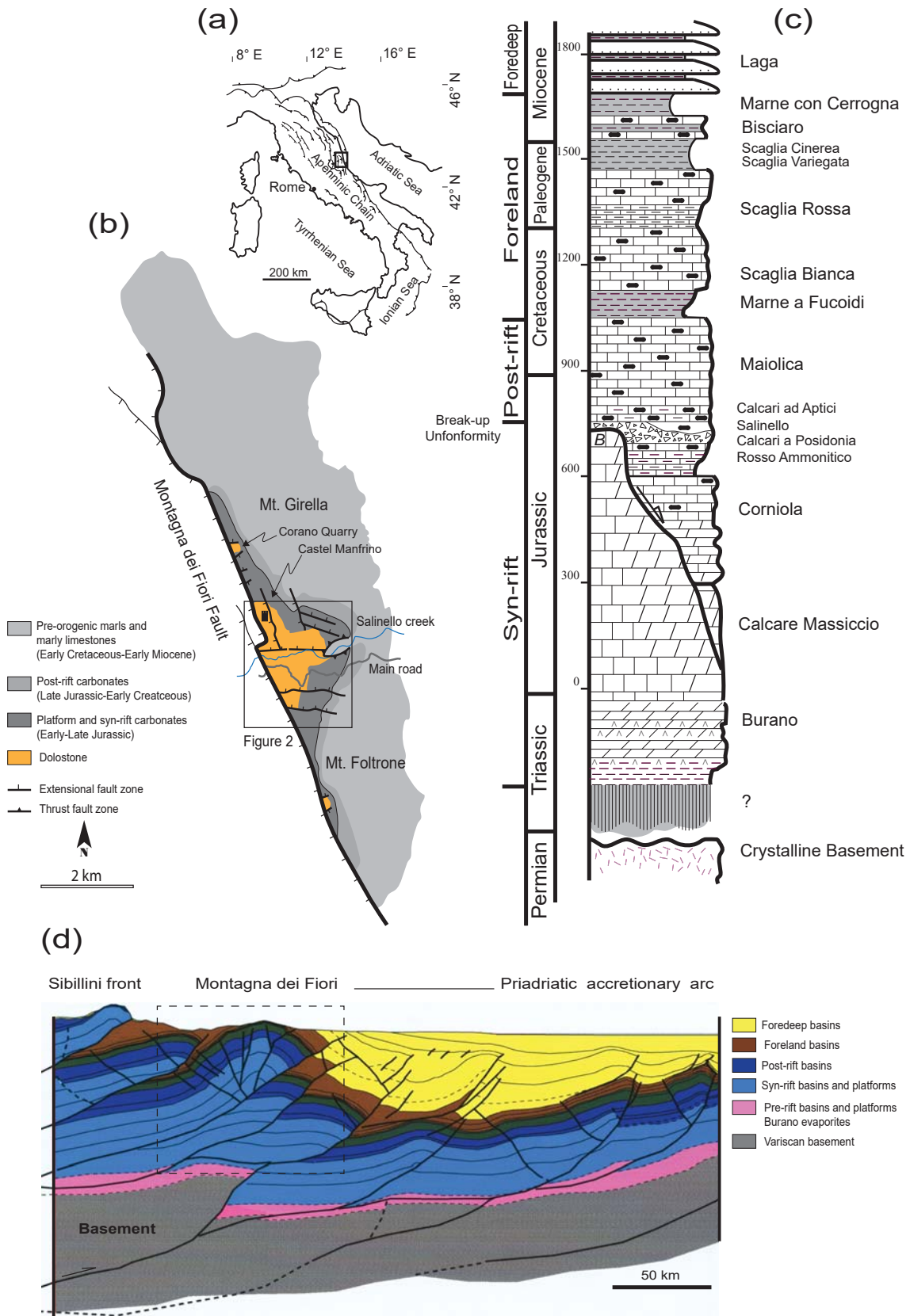


Fig. 1

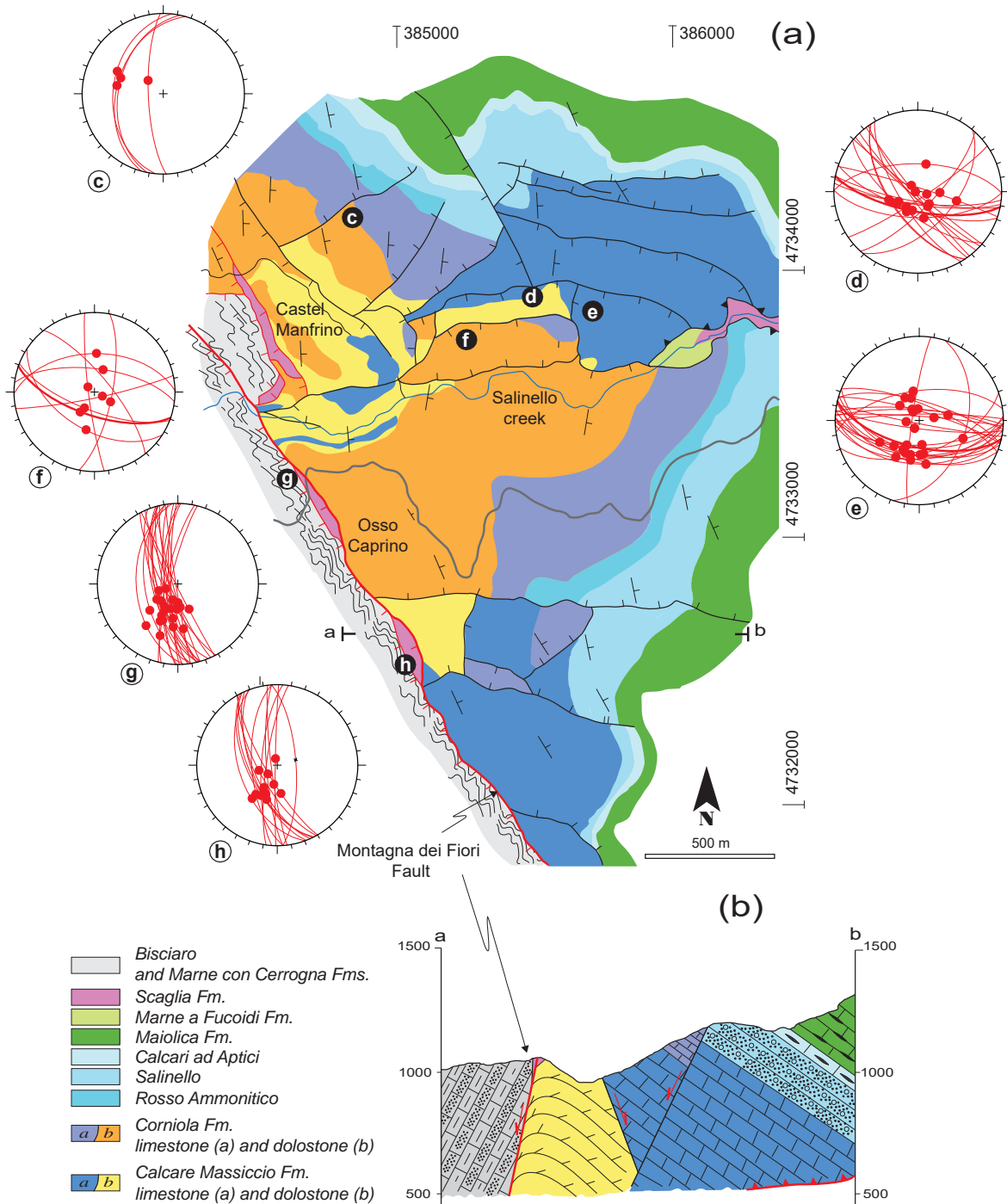


Fig. 2

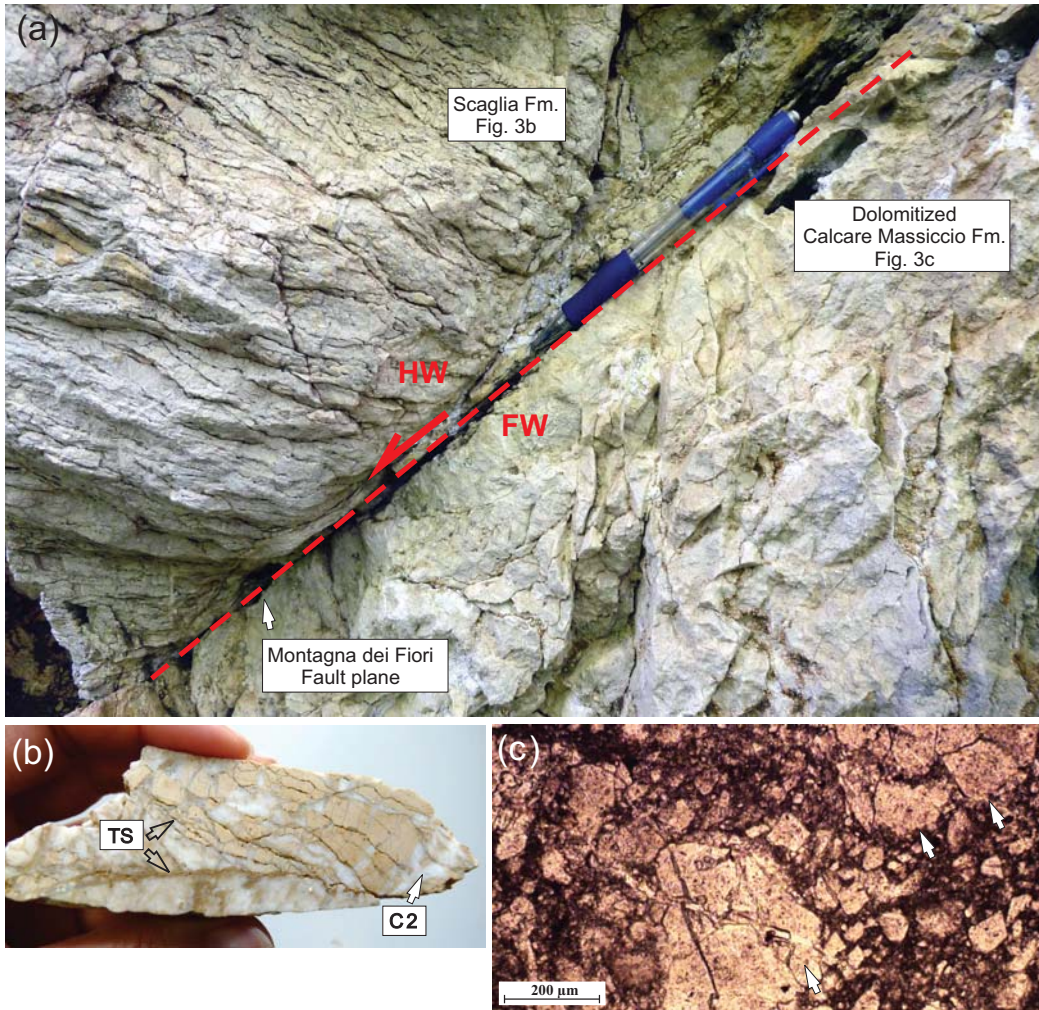


Fig. 3

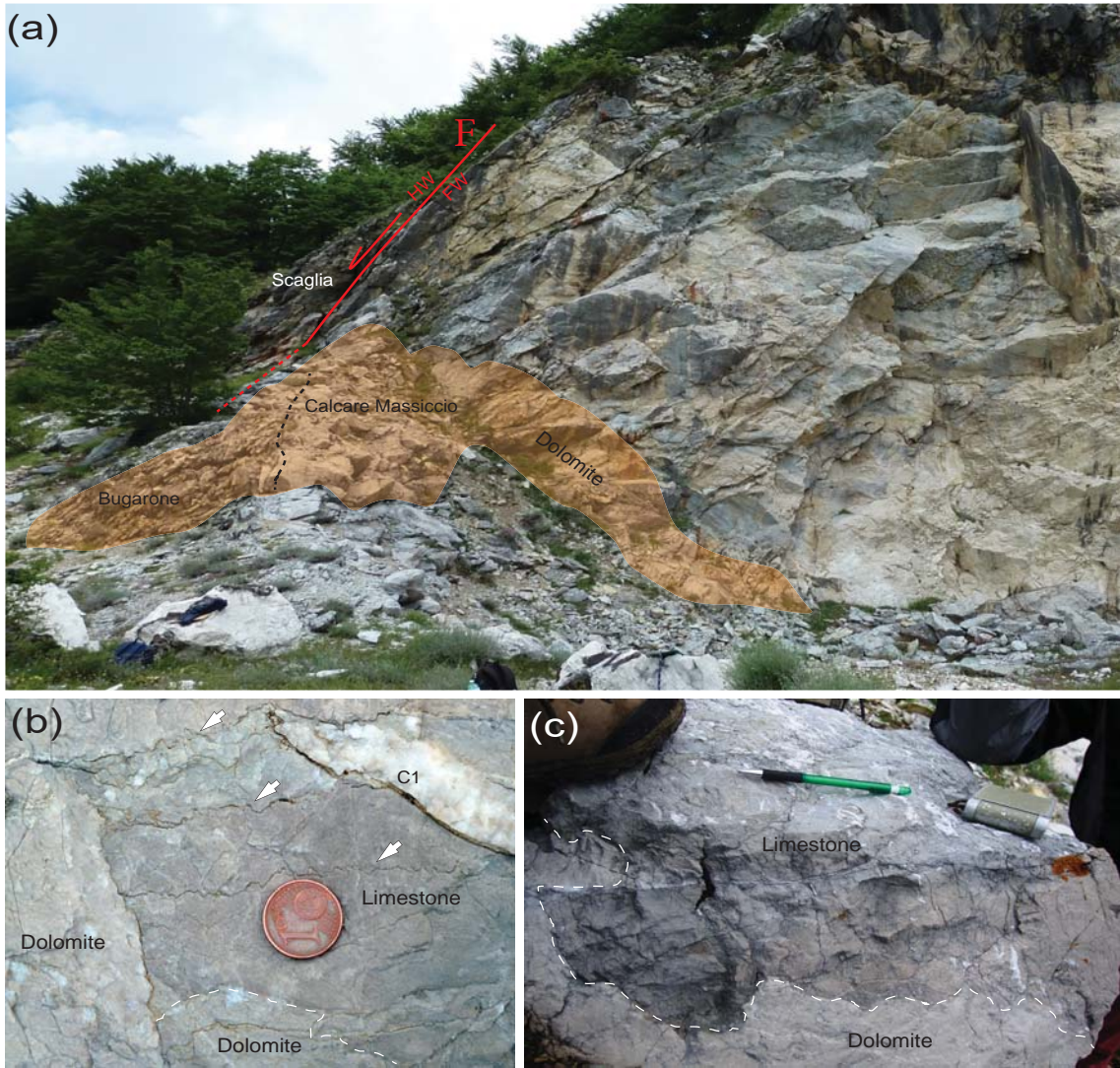


Fig. 4

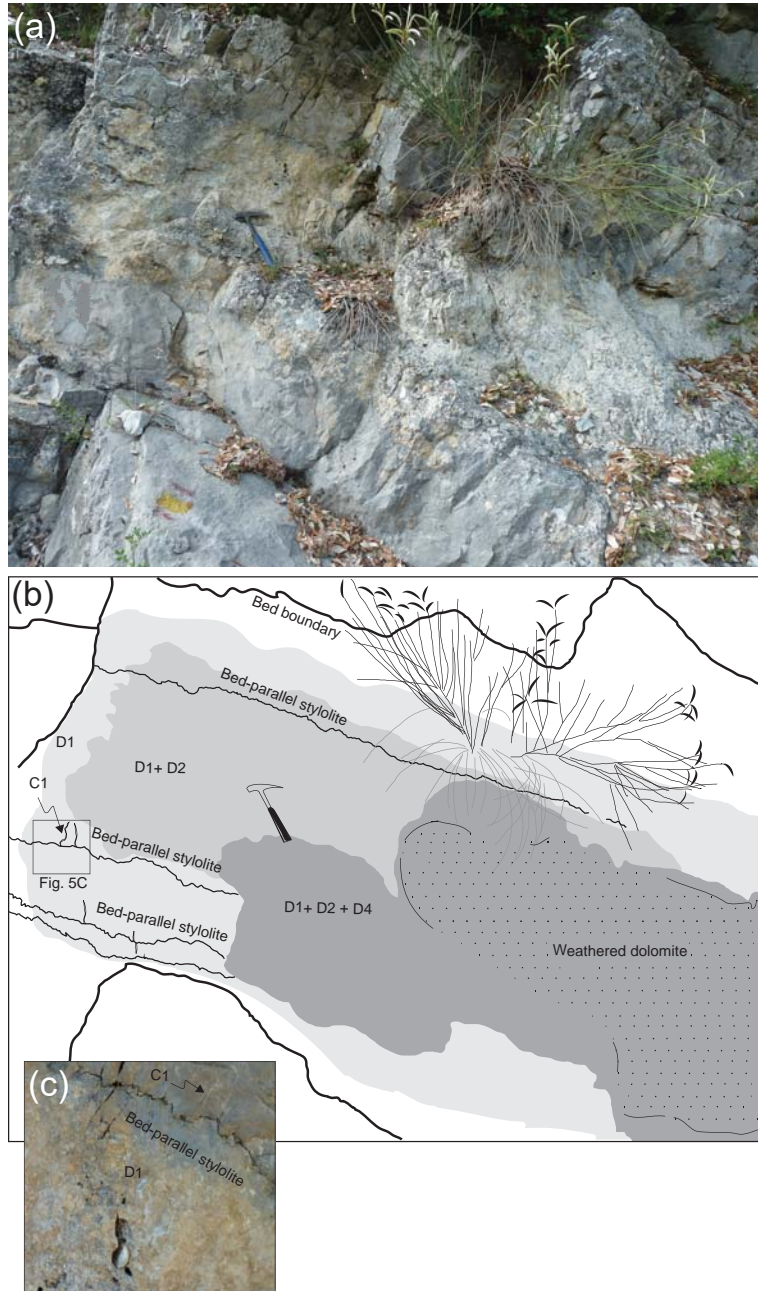


Fig. 5

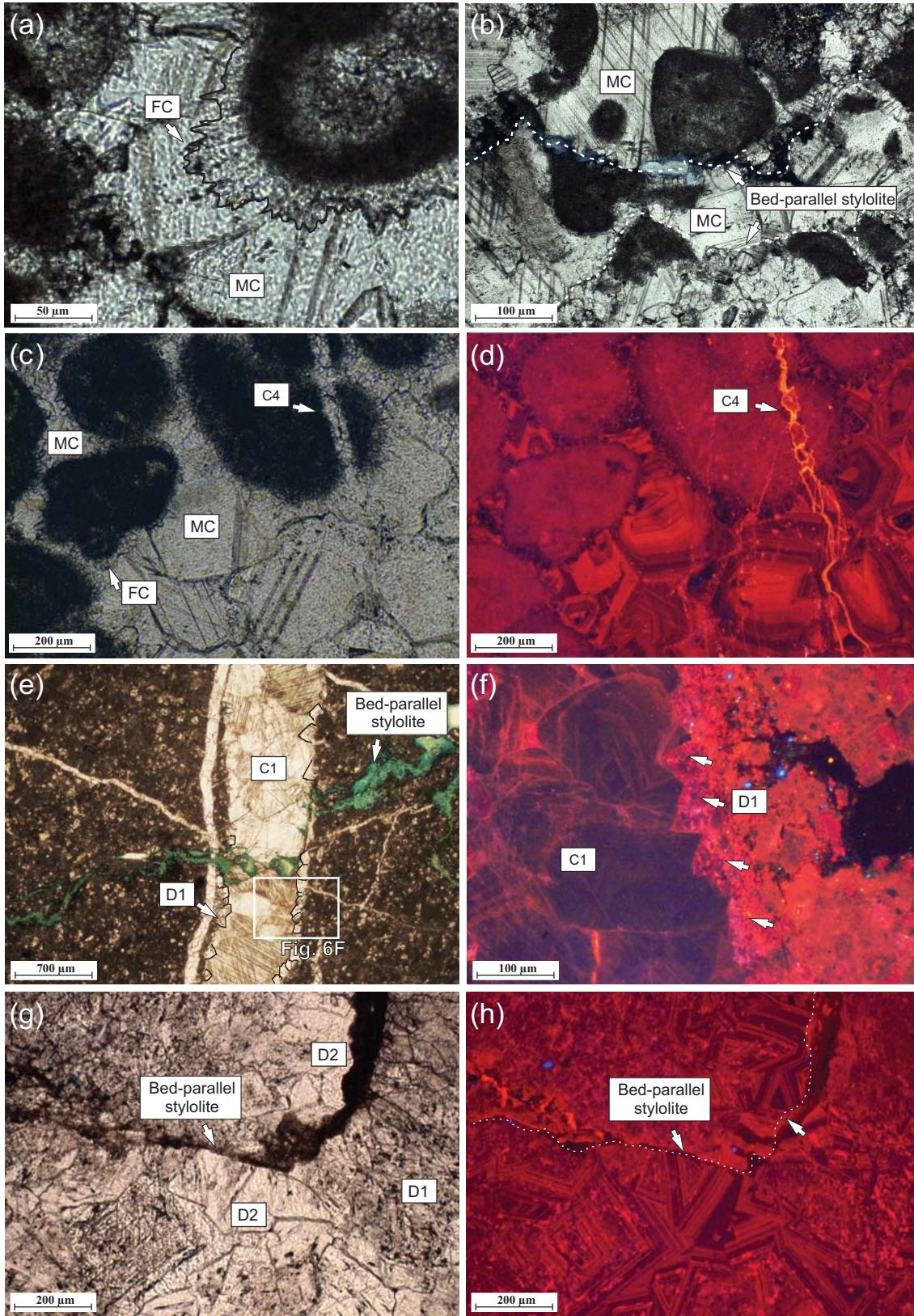


Fig. 6

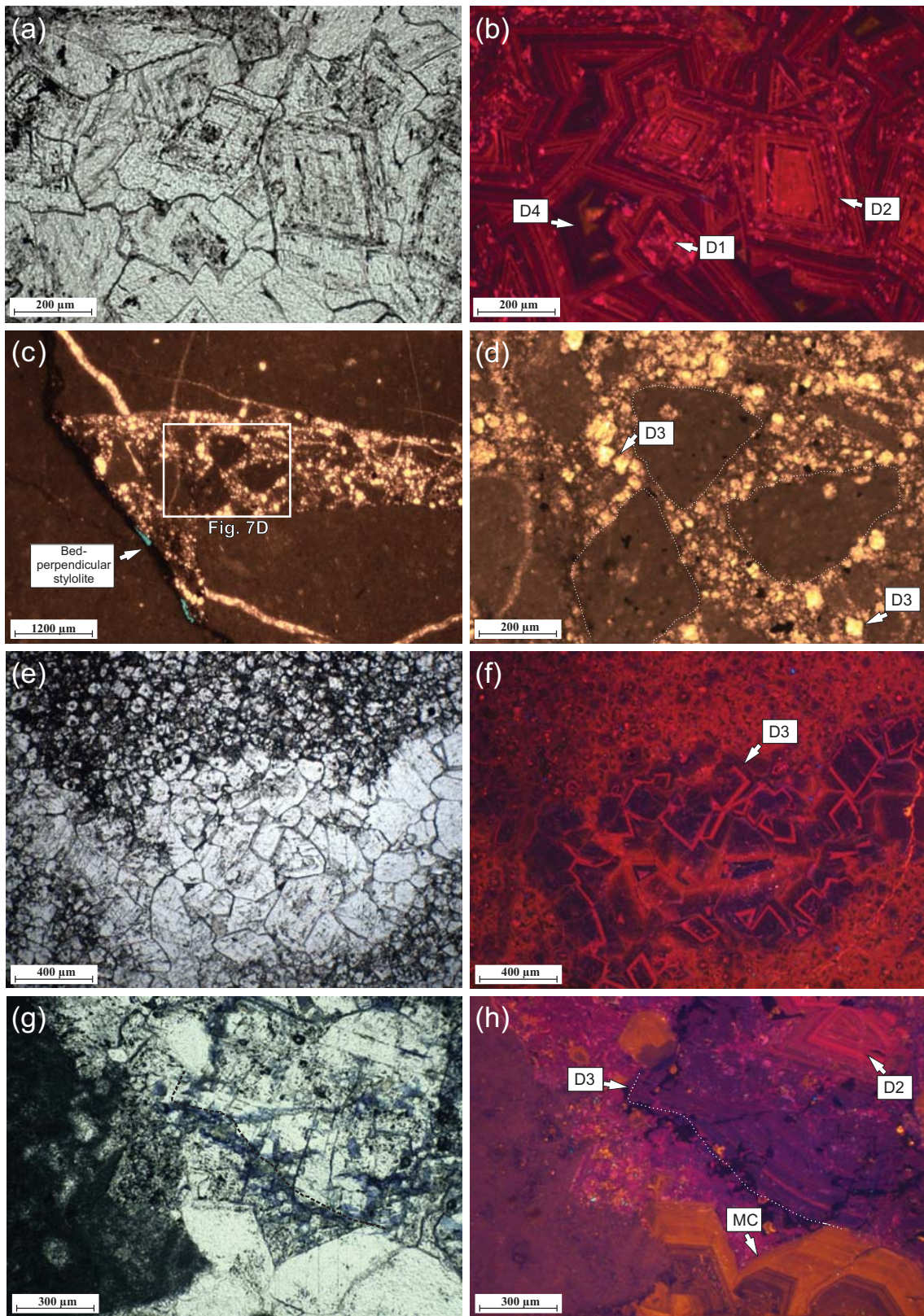


Fig. 7

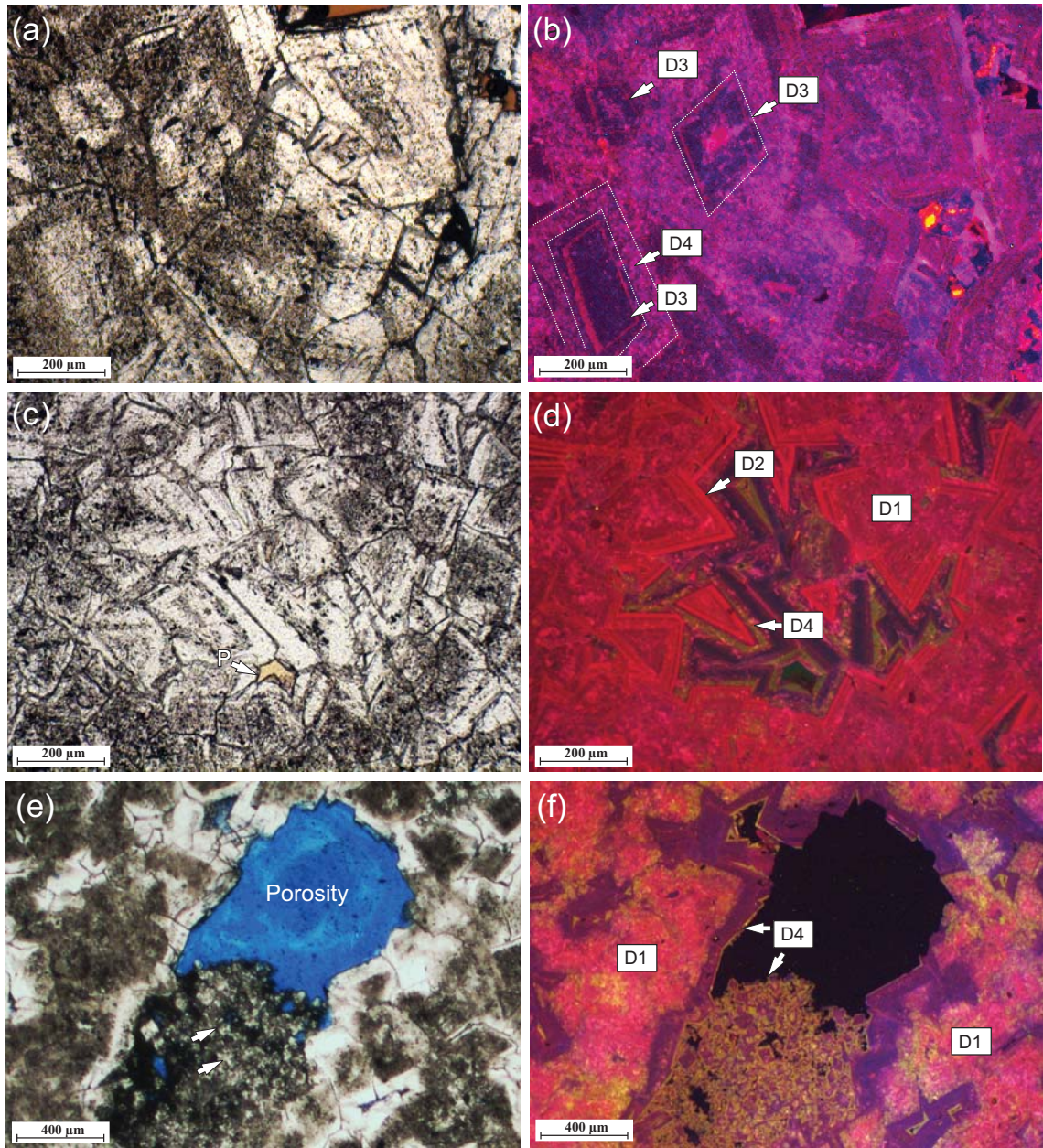


Fig. 8

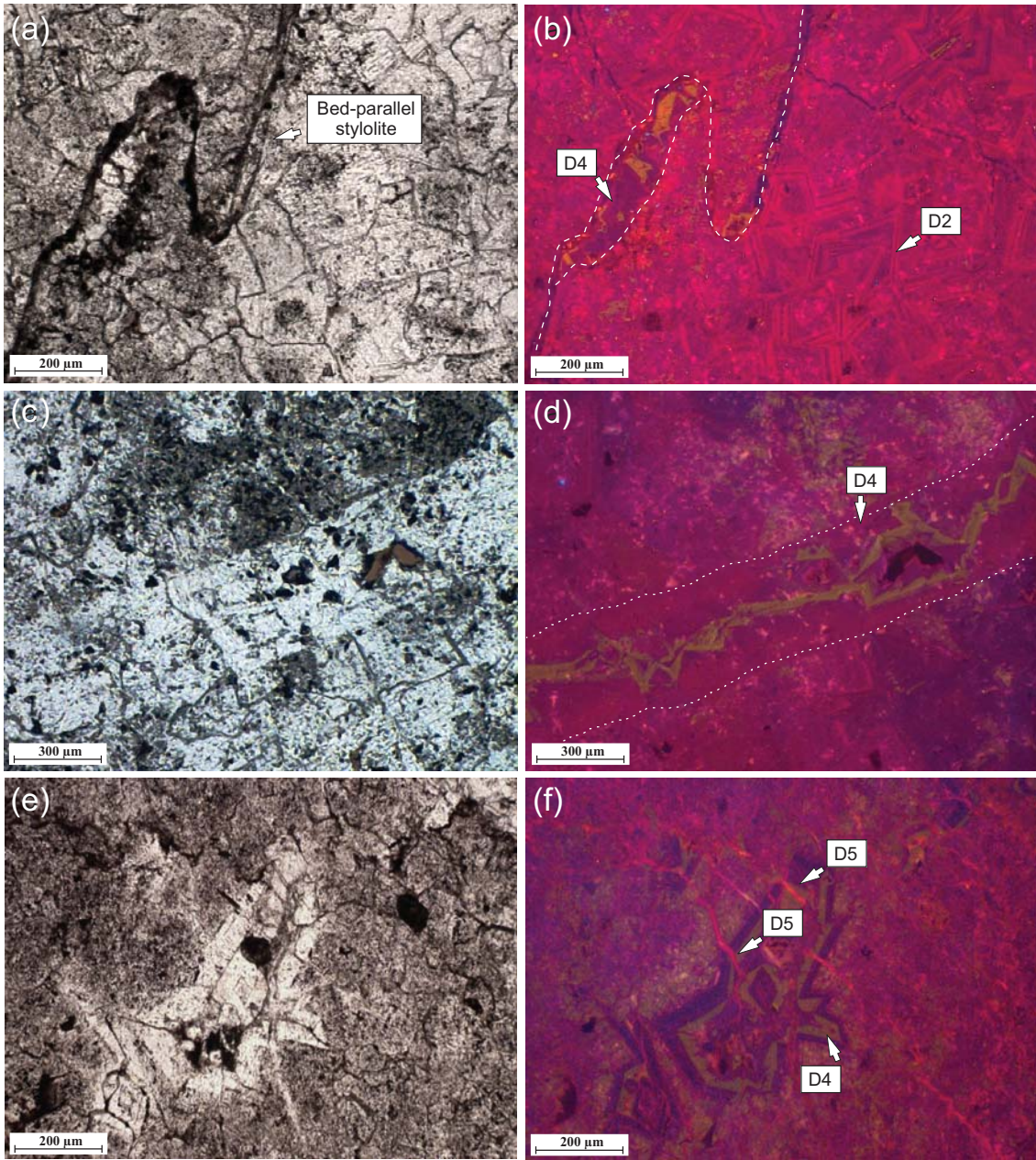


Fig. 9

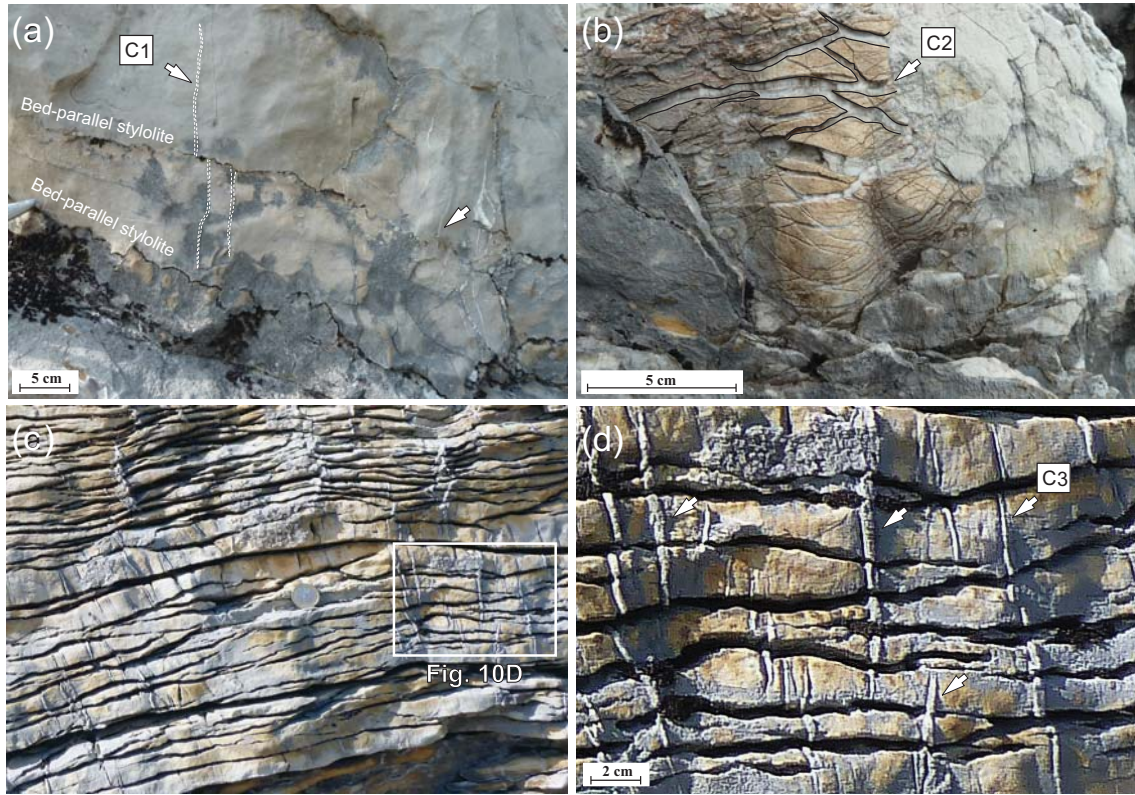


Fig. 10

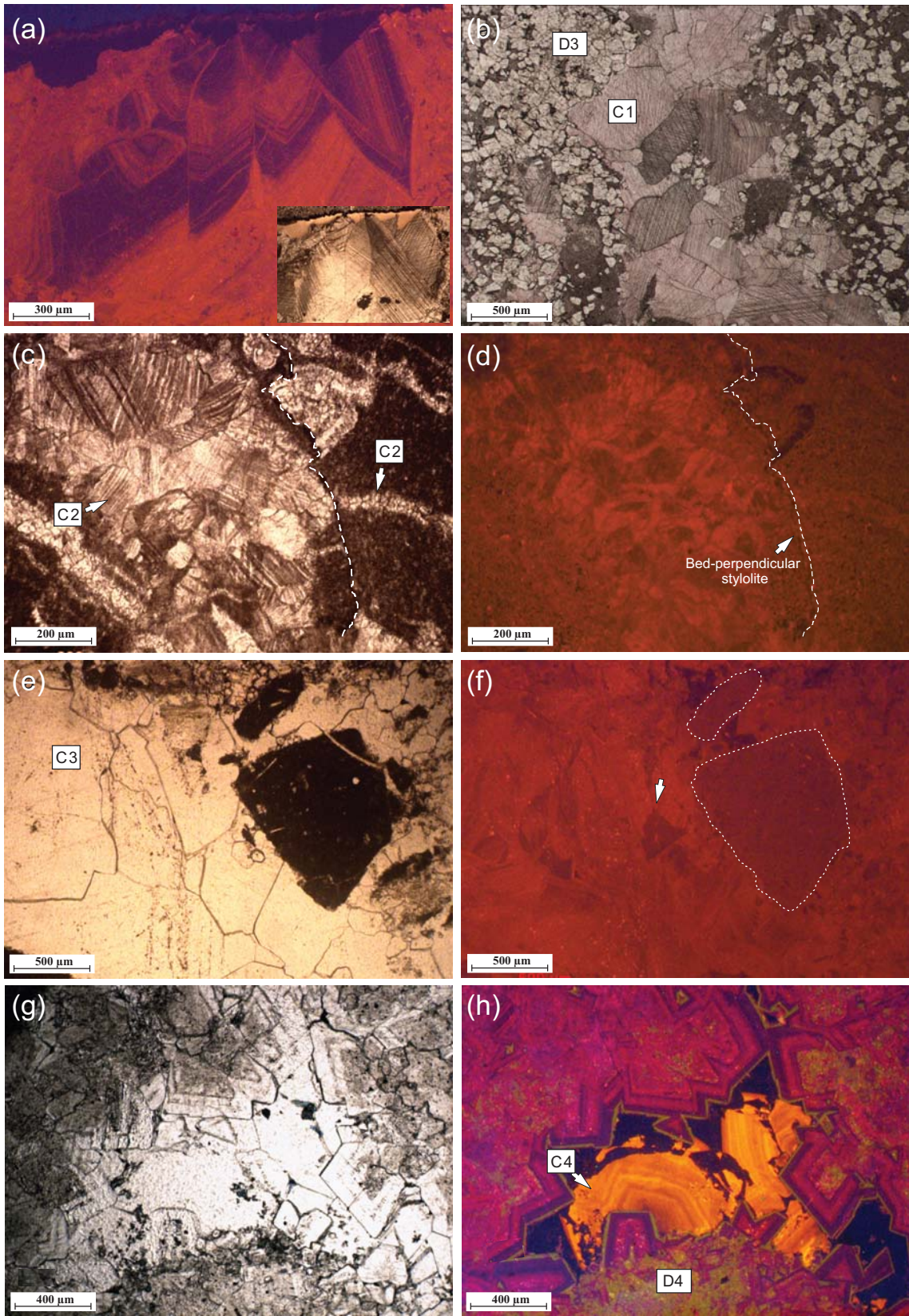


Fig. 11

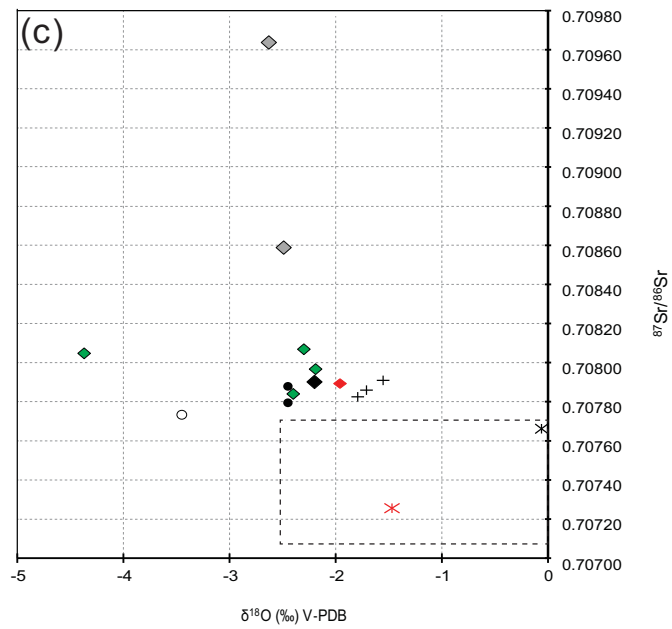
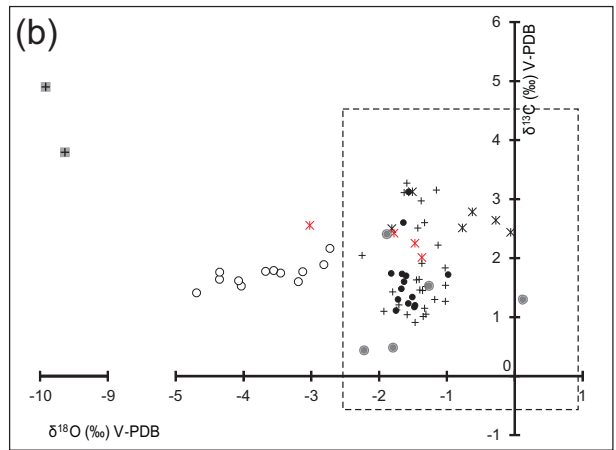
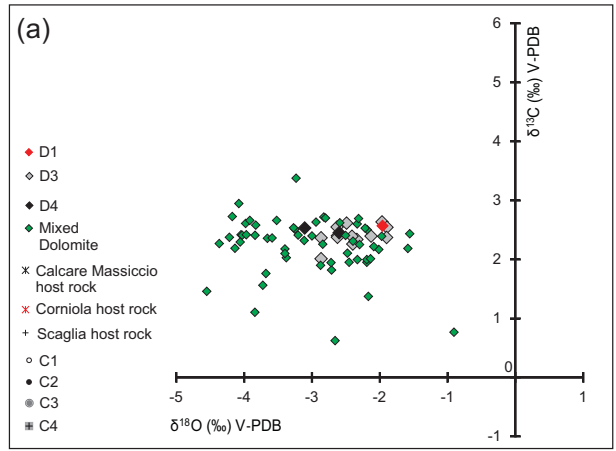


Fig. 12

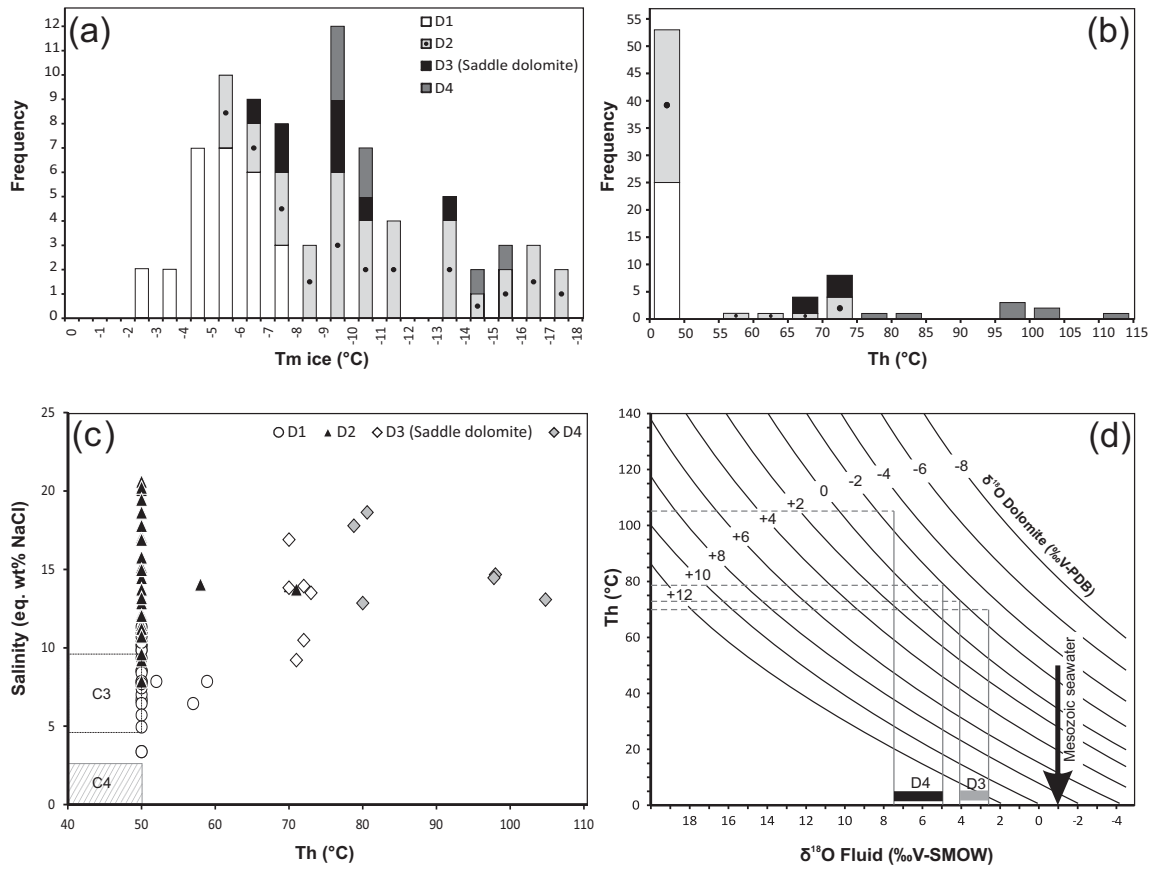


Fig. 13

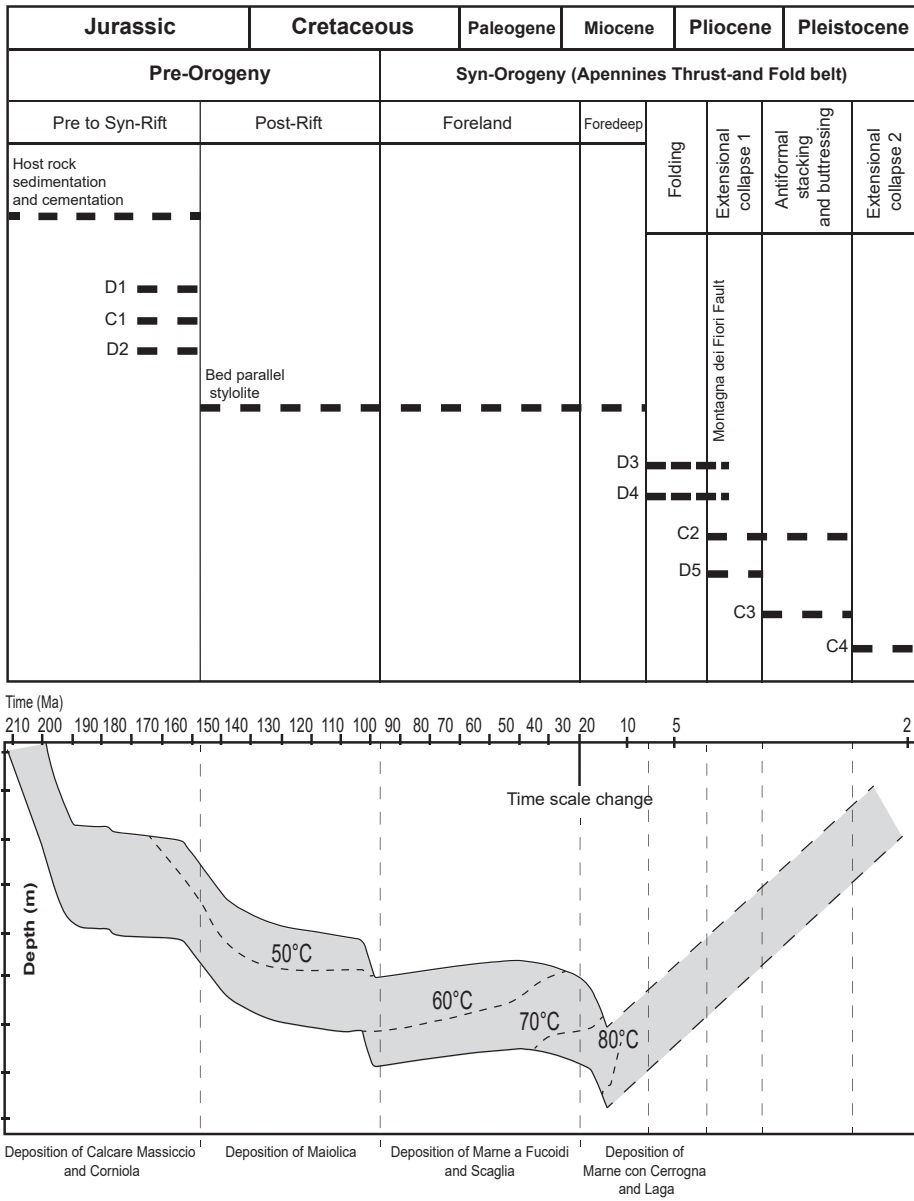


Fig. 14

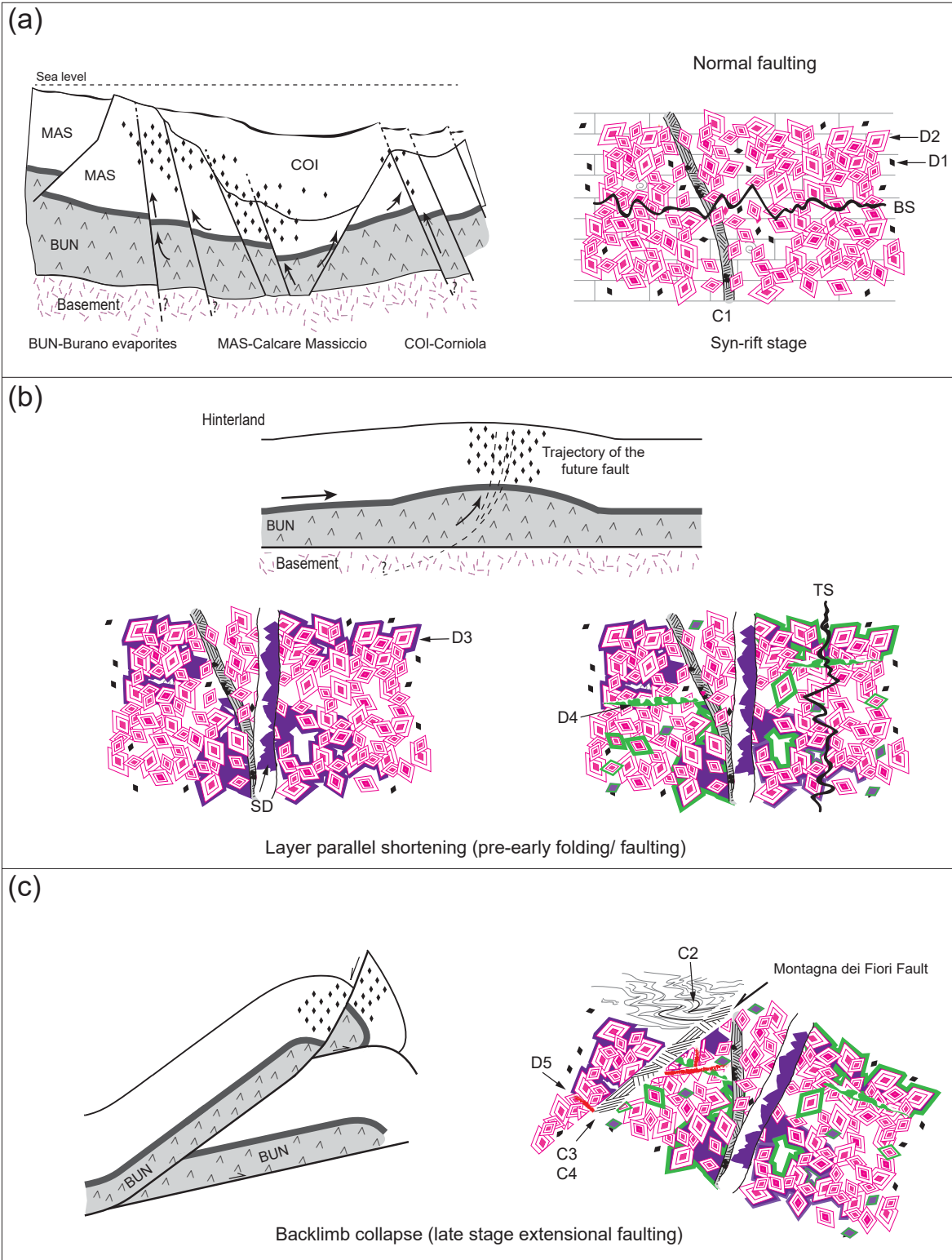


Fig. 15